The Rotation and Galactic Kinematics of Mid M Dwarfs in the Solar Neighborhood

The Astrophysical Journal, 821:93 (21pp), 2016 April 20 doi:10.3847/0004-637X/821/2/93

THE ROTATION AND GALACTIC KINEMATICS OF MID M DWARFS IN THE SOLAR NEIGHBORHOOD

Elisabeth R. Newton[1], Jonathan Irwin[1], David Charbonneau[1], Zachory K. Berta-Thompson[2], Jason A. Dittmann[1], and Andrew A. West[3]
[1] Harvard-Smithsonian Center for Astrophysics, 60 Garden Street, Cambridge, MA 02138, USA
[2] Kavli Institute for Astrophysics and Space Research and Department of Physics, Massachusetts Institute of Technology, Cambridge, MA 02139, USA
[3] Department of Astronomy, Boston University, 725 Commonwealth Avenue, Boston, MA 02215, USA
Received 2015 November 2; accepted 2016 February 5; published 2016 April 14

ABSTRACT

Rotation is a directly observable stellar property, and it drives magnetic field generation and activity through a magnetic dynamo. Main-sequence stars with masses below approximately $0.35\,M_{\odot}$ (mid-to-late M dwarfs) are fully convective, and are expected to have a different type of dynamo mechanism than solar-type stars. Measurements of their rotation rates provide insight into these mechanisms, but few rotation periods are available for these stars at field ages. Using photometry from the MEarth Project, we measure rotation periods for 387 nearby, mid-to-late M dwarfs in the northern hemisphere, finding periods from 0.1 to 140 days. The typical rotator has stable, sinusoidal photometric modulations at a semi-amplitude of 0.5%–1%. We find no period–amplitude relation for stars below $0.25\,M_{\odot}$ and an anticorrelation between period and amplitude for higher-mass M dwarfs. We highlight the existence of older, slowly rotating stars without Hα emission that nevertheless have strong photometric variability. We use parallaxes, proper motions, radial velocities, photometry, and near-infrared metallicity estimates to further characterize the population of rotators. The Galactic kinematics of our sample is consistent with the local population of G and K dwarfs, and rotators have metallicities characteristic of the solar neighborhood. We use the W space velocities and established age–velocity relations to estimate that stars with $P < 10$ days have ages of on average <2 Gyr, and that those with $P > 70$ days have ages of about 5 Gyr. The period distribution is dependent on mass: as the mass decreases, the slowest rotators at a given mass have longer periods, and the fastest rotators have shorter periods. We find a lack of stars with intermediate rotation periods, and the gap between the fast and slow rotators is larger for lower masses. Our data are consistent with a scenario in which these stars maintain rapid rotation for several gigayears, then spin down quickly, reaching periods of around 100 days by a typical age of 5 Gyr.

Key words: stars: kinematics and dynamics – stars: low-mass – stars: rotation – starspots

Supporting material: figure set, machine-readable table

1. INTRODUCTION

Rotation is one of the few directly observable stellar properties, and these observations provide constraints on the angular momentum evolution of stars. Late-time angular momentum loss is governed by magnetized stellar winds, which depend on the magnetic field topology. Stellar rotation therefore provides empirical insight into both the stellar wind and magnetic field. These interlinked properties are also relevant to the detection and characterization of their planetary systems. Stellar winds and magnetic fields affect habitability, potentially stripping the planetary atmosphere (Cohen et al. 2014). Rapidly rotating, active stars are also difficult targets for exoplanet surveys. Line broadening from the most rapidly rotating stars and radial velocity signals induced by stellar activity pose challenges for radial velocity surveys (Saar & Donahue 1997; Saar et al. 1998). In transit surveys, periodic modulations from starspots can cause confounding signals (e.g., Berta et al. 2012).

The rotation of fully convective stars (with $M < 0.35\,M_{\odot}$; Chabrier & Baraffe 1997) and of those that have an outer convective envelope depends on both age and mass. Stars spin up as they approach the zero-age main sequence, a consequence of Kelvin–Helmholtz contraction and late-stage accretion, and the conservation of angular momentum. To match the rotation periods observed in the youngest clusters, pre-main-sequence stars must also experience early angular momentum losses (e.g., Hartmann & Stauffer 1989; Bouvier et al. 1997). This is thought to be the result of star–disk interactions (e.g., Koenigl 1991; Collier Cameron et al. 1995; Matt & Pudritz 2005). After stars reach the main sequence, angular momentum loss is dominated by magnetized stellar winds, the strength of which may depend on mass. By the age of the Hyades, the rotation periods of solar-type dwarfs have reached a narrow range and subsequently obey a Skumanich-type relation (Skumanich 1972) between angular velocity (ω), mass, and age (t), where $\omega \propto t^{-1/2}$. The well-defined rotation–age relation and the lack of dependence on initial conditions gives rise to the concept of gyrochronology (Barnes 2003).

The convergence of stellar rotation periods can be described by a parameterized wind-loss model (Kawaler 1988; Reiners & Mohanty 2012b), in which more rapid rotators spin down faster. The rate of angular momentum loss is thought to saturate for stars with angular velocities faster than some mass-dependent critical value $\omega_{\rm sat}$. This is typically modeled as a change in how the angular momentum loss rate depends on rotation rate, which occurs when the angular velocity drops below the critical value. This leads to a change in the time dependence of the rotation rate itself. In the most common prescription (e.g., Bouvier et al. 1997), during the saturated regime (rapid rotation), ω decreases exponentially with time, and in the unsaturated regime, ω follows the Skumanich law. This behavior causes the rotation periods to converge as the stars evolve from the saturated to unsaturated regime. The well-

behaved relationship between rotation, age, and color for solar-type stars with ages greater than roughly 650 Myr can be used to infer ages of isolated field stars through gyrochronology, by measuring their rotation period and color.

For solar-type stars, angular momentum evolution can be modeled with reasonable success using currently available observations. However, these models may not be able to simultaneously fit the evolution of the lowest-mass dwarfs (e.g., Irwin et al. 2011; Reiners & Mohanty 2012b). This could arise from a different magnetic dynamo in fully convective stars. Models of the solar magnetic dynamo indicate the importance of stellar rotation in the generation of the solar magnetic field (see Charbonneau 2005 for a review). The tachocline, the interface between the radiative and convective zones, has also been thought to be key. In some solar dynamo models, the tachocline is where the strengthening and organization of the solar magnetic field occurs. The tachocline is not present in fully convective stars; nevertheless, strong magnetic fields appear to be prevalent among these low-mass stars (Johns-Krull & Valenti 1996; Reiners & Basri 2010). Theoretical models of magnetic dynamos in fully convective stars focus on how rotation and convection can maintain a magnetic field in the absence of a tachocline (e.g., Chabrier & Küker 2006; Dobler et al. 2006; Browning 2008; Yadav et al. 2015).

Measurements of stellar rotation provide insight into angular momentum evolution and the magnetic dynamo. Observational constraints at young ages come predominantly from open clusters and moving groups, with ages from a few Myr (e.g., the Orion Nebular Cluster) to that of the Hyades and Praesepe (625 Myr; Perryman et al. 1998; Gáspár et al. 2009; Bell et al. 2014). The Sun and the old stellar clusters NGC 6811 (1 Gyr) and NGC 6819 (2.5 Gyr) provide anchors at greater ages for stars around solar mass (Meibom et al. 2011, 2015). While solar-mass stars have converged to a narrowly constrained mass–rotation relation by 650 Myr, M dwarfs still show a broad range of rotation rates at this age and continue to undergo substantial angular momentum evolution at field ages. Observations of *field* M dwarfs are therefore particularly important for constraining their angular momentum evolution. Substantial observational progress has been made in recent years, with many new measurements of rotation periods for field M dwarfs, notably by Kiraga & Stępień (2007, 2013), Norton et al. (2007), Hartman et al. (2011), Irwin et al. (2011), Kiraga (2012), Goulding et al. (2013), and McQuillan et al. (2013).

Determining the ages of field stars is important for enabling their use in modeling rotational evolution. The radii and effective temperatures of M dwarfs remain mostly unchanged once they reach the main sequence and therefore do not provide robust constraints on their ages. Galactic kinematics provide one possible approach. The motions of stars through the solar neighborhood bear signatures of their past dynamical interactions. Stars form in dense clusters with kinematics generally constrained to a co-rotating disk with a small scale height and a small velocity dispersion. After their formation, there are two primary effects on the stars' kinematics: the clusters dissipate and stars undergo dynamical heating. Most clusters are not gravitationally bound and evaporate over time, although some physically associated, coeval stellar populations persist as the young moving groups and open clusters mentioned previously. Dynamical interactions increase the velocity dispersion of a group of stars over time. This mechanism acts within the kinematically cold stellar population known as the "thin disk," and also is thought to have produced the population of kinematically hotter stars often referred to as the "thick disk." Whether the thick disk should be described by a single population or a superposition of many mono-age or mono-abundance populations has recently been called into question (Bovy et al. 2012; Minchev et al. 2015), but it is composed of stars generally older than, and with different chemical abundances from, the canonical thin disk (Bensby et al. 2005). Within the thin/young disk, the velocity dispersion increases with age. Relationships between age and velocity dispersion have been calibrated for stars in the solar neighborhood (e.g., Wielen 1977; Nordstrom et al. 2004). Kinematics can therefore shed light on the ages of *populations* of stars.

Irwin et al. (2011) contributed a substantial number of the currently available measurements for fully convective stars, with rotation periods for 41 M dwarfs from the MEarth transit survey (Berta et al. 2012; Irwin et al. 2014) that had published trigonometric parallaxes. By assigning stars to the thin/young and thick/old disk based on their space velocities, we showed that the rapidly rotating M dwarfs were on average younger than the slowly rotating stars.

In this work, we extend the analysis of Irwin et al. (2011) to the full northern sample of M dwarfs observed by MEarth. Our sample is particularly of interest due to the large body of observations that our team has gathered on these stars. We measured parallaxes for 1507 of the MEarth targets using MEarth astrometry (Dittmann et al. 2014) and calibrated the MEarth photometric bandpass to provide optical magnitudes for every target (Dittmann et al. 2016). In Newton et al. (2014), we obtained low-resolution near-infrared spectra of 447 MEarth targets, measuring their absolute radial velocities (RVs) and estimating their iron abundances ([Fe/H]). Using the Hα line to trace magnetic activity and additional rotation periods derived from MEarth data, we found that the fraction of active stars continues to decrease with increasing rotation period out to the longest rotation periods in the MEarth sample (West et al. 2015).

2. PHOTOMETRY FROM MEARTH

The MEarth Project is an all-sky transit survey searching for planets around approximately 3000 nearby, mid-to-late M dwarfs (Berta et al. 2012; Irwin et al. 2014). MEarth-North is located at the Fred Lawrence Whipple Observatory, on Mount Hopkins, Arizona, and has been operational since 2008 September. MEarth-South, at Cerro Tololo Inter-American Observatory (CTIO) in Chile, was commissioned in 2014 January. Each installation consists of eight 40 cm telescopes on German Equatorial Mounts, equipped with CCD cameras. This work uses data from only MEarth-North.

Nutzman & Charbonneau (2008) selected the northern MEarth targets from the northern proper motion catalog of Lépine & Shara (2005), which includes stars with proper motions $>0\farcs15\,\mathrm{yr}^{-1}$. MEarth exclusively targets nearby, mid-to-late M dwarfs: at the time of selection, all stars had parallaxes or distance estimates (spectroscopic or photometric; Lépine 2005) placing them within 33 pc, and estimated stellar radii less than $0.33\,R_{\odot}$. Trigonometric parallaxes are now available for the majority of stars in the northern sample (Dittmann et al. 2014).

MEarth targets are spread across the sky and must therefore be targeted individually; targets are visited at a cadence of 20–30 minutes for observations taken as part of the main planetary transit search. Additional observations of all targets have been taken at a cadence of approximately 10 days since 2011 September for the astrometric program (Dittmann et al. 2014, 2016). We include these data in the analysis presented here. Exposure times are set for each object such that a transit by a planet of two Earth radii would be detected in each datum at 3σ, and they therefore depend on the estimated stellar radii. We use the mass–M_K relation of Delfosse et al. (2000) to estimate stellar masses, then the mass–radius polynomial of Bayless & Orosz (2006) to estimate stellar radii. Our current exposure time calculations also use the trigonometric distances from Dittmann et al. (2014). We did not adjust the exposure time of individual images when we updated the stellar parameters in order to avoid changing the effect of nonlinearity on our photometry; instead, we co-add exposures to reach the requisite sensitivity when necessary. Each visit to a star may therefore contain multiple exposures.

Northern target stars are typically observed at the cadence of 20–30 minutes for one to two observing seasons, with each season lasting from mid-September of one year to mid-July of the following year. During southern Arizona's summer monsoons, MEarth-North is shut down completely.

For the 2008–2009 and 2009–2010 observing seasons, we used long-pass filters composed of 5 mm thick Schott RG715 glass. In 2010–2011, in an attempt to mitigate color-dependent systematics (discussed at the close of this section and in Irwin et al. 2006), we switched to a custom filter with a sharp interference cutoff at the red end, approximating the Cousins *I*-band. Finding that this increased the level of systematics rather than mitigating them, we reverted to RG715 filters from 2011–2012 onwards, but with 3 mm thickness.

We do not attempt to stitch observations taken with different filters or different telescopes together, so the data on each star may be composed of multiple light curves, where we define a *light curve* as the set of observations from a single MEarth telescope with a single filter setup. A single light curve will therefore contain data from one of the 2008–2010, 2010–2011, or 2011–2015 intervals. Each object is usually assigned to a single telescope for the entirety of its observations; however, starting in the 2012–2013 season, two telescopes were assigned to a subset of the targets (see Berta et al. 2012). A small number of targets also appear in multiple fields (where there are multiple targets within the field of view) so may have more light curves.

For our data reduction, we follow the methodology of Irwin et al. (2006), modified for the specifics of the MEarth data as detailed in Berta et al. (2012). We highlight here several systematics that affect our ability to detect rotation periods:

1. Irwin et al. (2011) noted weather-dependent effects in the differential magnitudes of the target M dwarfs, which result from variations in telluric water vapor absorption in the bandpass of the RG715 filter, or humidity dependence of the interference cutoff in the interference filters used in 2010–2011. Because our targets are typically the only M dwarfs in the field, the reference stars predominantly have bluer colors. Therefore, the observed fluxes of the targets and reference stars are affected differently by the varying telluric absorption or humidity when integrated over the filter bandpass. This effect cannot be corrected with standard differential photometry procedures, and we note that the resulting systematic effects are dominated by the time variability of the driving quantity (precipitable water vapor or humidity) and are not strongly correlated with airmass, so cannot be corrected by standard methods for removing atmospheric extinction. Instead, the differential magnitudes of all of the M dwarfs being observed within a half-hour window are combined to produce a comparison light curve of lower cadence, which we call the "common mode," that measures any residual photometric variations that are common to the target M dwarfs. Due to differences in the target spectral types, it is necessary to scale the common mode by a factor that varies for each object. This scale factor has proved difficult to calculate, so it is fit empirically from the light curve.
2. The MEarth telescopes use German Equatorial Mounts, which require the telescope tube to be flipped over the pier when the target crosses the meridian, resulting in rotation of the focal plane relative to the sky by 180°, and causing stars to sample two distinct regions of the detector. Residual flat-fielding errors result in offsets in the differential magnitudes between the two locations. To correct for this, we assign a different baseline magnitude to observations taken at these two rotation angles. Additional flat-fielding errors are inevitably introduced whenever the cameras are removed from the telescopes for repair, so we introduce a new pair of baseline magnitudes each time this is done. We refer to the set of data taken between these camera removals on a single side of the meridian as a light curve "segment," where each segment is modeled with its own baseline magnitude when producing differential photometry.
3. The large-scale structure of our flat field evolves on timescales of several years. We take nightly twilight flats, but because the illumination is dominated by scattered light, we filter out all of the large-scale structure. To account for the large-scale flat-field structure, we observe a star field in the Galactic plane dithered randomly inside a box of one square degree, and use photometry to obtain the large-scale flat-field pattern. These observations require a substantial amount of telescope time during photometric conditions, so are repeated only intermittently. We have used a single large-scale correction for each of the 2008–2010, 2010–2011, and 2011–2015 data sets, in order to avoid introducing spurious signals when there are sudden changes in this correction. However, there are several instances where rapid evolution in the flat field is evident, which we account for by introducing additional segments with new baseline magnitudes.

We discuss our treatment of these systematics during determination of the rotation period in the following section.

3. DETERMINING ROTATION PERIODS

We attempt to identify rotation periods in each of the 1883 targets observed with MEarth-North, including data obtained through 2015 August 16.

3.1. Period Detection

We apply the method used by Irwin et al. (2011), which is based on Irwin et al. (2006), to fit simultaneously for terms

needed to account both for our systematics and for rotational modulation. For each light curve, we fit both a null hypothesis, which assumes that the light curve has no astrophysical variability and can be fit with systematics alone, and an alternative hypothesis that includes a sinusoid.

Our models include two terms to address the two systematics discussed in the previous section: the common mode, and the baseline magnitude in each segment of the light curve.

The null model takes the form

$$m_{\rm null}(t) = m_i + k\, c(t) \quad (1)$$

where i is the segment number, m_i is the baseline magnitude for segment i of the light curve, t is time and k scales the common mode $c(t)$. We include only as many m_i constants as there are segments containing data points, so for example if a target was observed only on one side of the meridian, only a single baseline magnitude is fit. This model corresponds to a constant intrinsic magnitude (above the Earth's atmosphere) for the target M dwarf, modulated by the atmospheric and instrumental systematics.

The alternative model additionally includes a sinusoid:

$$m_{\rm alt}(t) = m_{\rm null}(t) + a\, \sin(\omega t + \phi) \quad (2)$$

where a is the semi-amplitude (in magnitudes), ϕ is the phase, and ω is the angular frequency $\omega = 2\pi/P$, where the rotation period is given by P. For fitting purposes, we rewrite the sine term on the right-hand side of this equation using standard trigonometric identities to replace the nonlinear ϕ parameter with a pair of linear semi-amplitudes a_s and a_c:

$$m_{\rm alt}(t) = m_{\rm null}(t) + a_s\, \sin(\omega t) + a_c\, \cos(\omega t). \quad (3)$$

Observations of a star may comprise several separate light curves. These are fit simultaneously, enforcing a common period over all light curves. The common mode scaling, baseline magnitudes, and the amplitude and phase of the sinusoid are independent. Before fitting, we remove data deviating from the median by more than 5σ, where we use the median absolute deviation scaled to the Gaussian-equivalent rms (Hoaglin et al. 1983) to define σ. Clipping is done to remove flares and (in some cases) eclipses, rather than to iteratively improve our fit by removing outliers. We do not use outlier removal in our fits because we are comparing models at different periods—each model could clip different data, and the χ^2 of poorly fitting models would be artificially reduced.

We use a maximum likelihood method to find the best-fitting rotation period under the assumption of the alternative hypothesis. We step through a uniformly spaced grid of frequencies corresponding to periods ranging from 0.1 to 1500 days, performing a linear least-squares fit of Equation (3) to the remaining variables at each frequency. As the null hypothesis is nested within the alternative, an F-test is appropriate for determining whether the addition of a sinusoid is warranted. We therefore calculate the F-test statistic (which measures the amount of variance that is explained by the additional parameters in the alternative model) at each frequency and select the one with the highest statistic as the candidate frequency. The set of F-test statistic values as a function of frequency are analogous to a periodogram.

We then visually inspect the light curves for each M dwarf, looking at the data with the common mode and varying baseline magnitudes removed. We look at differential magnitude as a function of time and at the data phased to the candidate frequency from the F-test. For some objects, multiple exposures were acquired at each visit in order to achieve the signal-to-noise ratio we require for planet detection. While fitting is performed on unbinned data, we visually examine the data both binned by visit and unbinned.

We assess the validity of the candidate period by posing a series of questions developed after early exploration of the data, but emphasize that the criteria we use in deciding whether a period is detected are fundamentally qualitative. The questions we ask are:

1. Can the candidate periodic rotation signal be seen by eye in the binned, phase-folded data?
2. Are two or more complete, near-consecutive rotation cycles seen? An important factor is the baseline magnitudes, which can allow data at disparate times to be offset arbitrarily; thus, data spanning multiple segments must be considered carefully.
3. Is the candidate rotation signal uncorrelated with systematics included in the model (baseline magnitude offsets and the common mode) and with the FWHM of the image?
4. If the candidate period is <10 days, can the variability be seen during single, well-sampled nights?
5. If there are simultaneously observed light curves, do the concurrent data agree?

After considering these questions, we classify objects as either "rotators" or "non-rotators." Rotators are objects that we consider to have secure detections of periodic photometric modulation that we assume to be attributable to stellar rotation. We further assign rotators a rating of "grade A" (274 stars) or "grade B" (113 stars). Grade A means that we are confident that we have identified a sinusoidal photometric modulation that can be attributed to an astrophysical source; the answer to all posed questions must be "yes." Grade B means that a modulation has been detected that we believe to be real, but that the signal does not pass all of our tests. Most grade B rotators fail only one criterion, and fall into one of the following categories: (1) two complete cycles are not seen, but the variability that is detected strongly suggests periodic modulation, (2) the only data available are from our astrometric program so the candidate periodicity is not sampled at high cadence, (3) a convincing period is detected, but the noise level is comparable to the amplitude of modulation.

Representative examples of grade A and B rotators are shown in Figure 1. The median of the phased data in ten equally spaced bins is also included. The sample scatter about the median (1.48 times the median absolute deviation) is shown, but is typically smaller than the data points.

We assign non-rotators a rating of either "possible/uncertain" (239 stars) or "no detection" (1260 stars). If we detect a candidate signal, but are not confident enough in its veracity to consider the object a rotator, we assign it a "possible" rating. A "no detection" rating indicates that we cannot positively identify a periodic modulation. Importantly, "no detection" does not mean that object is not rotating.

While we do not require a specific value for the F-test statistic, our rotators comprise most of the statistically significant peaks (Figure 2).

We present rotation period measurements for rotators with grade A and B ratings in Table 1. We do not attempt to assign errors in these periods (for example, based on the width of the

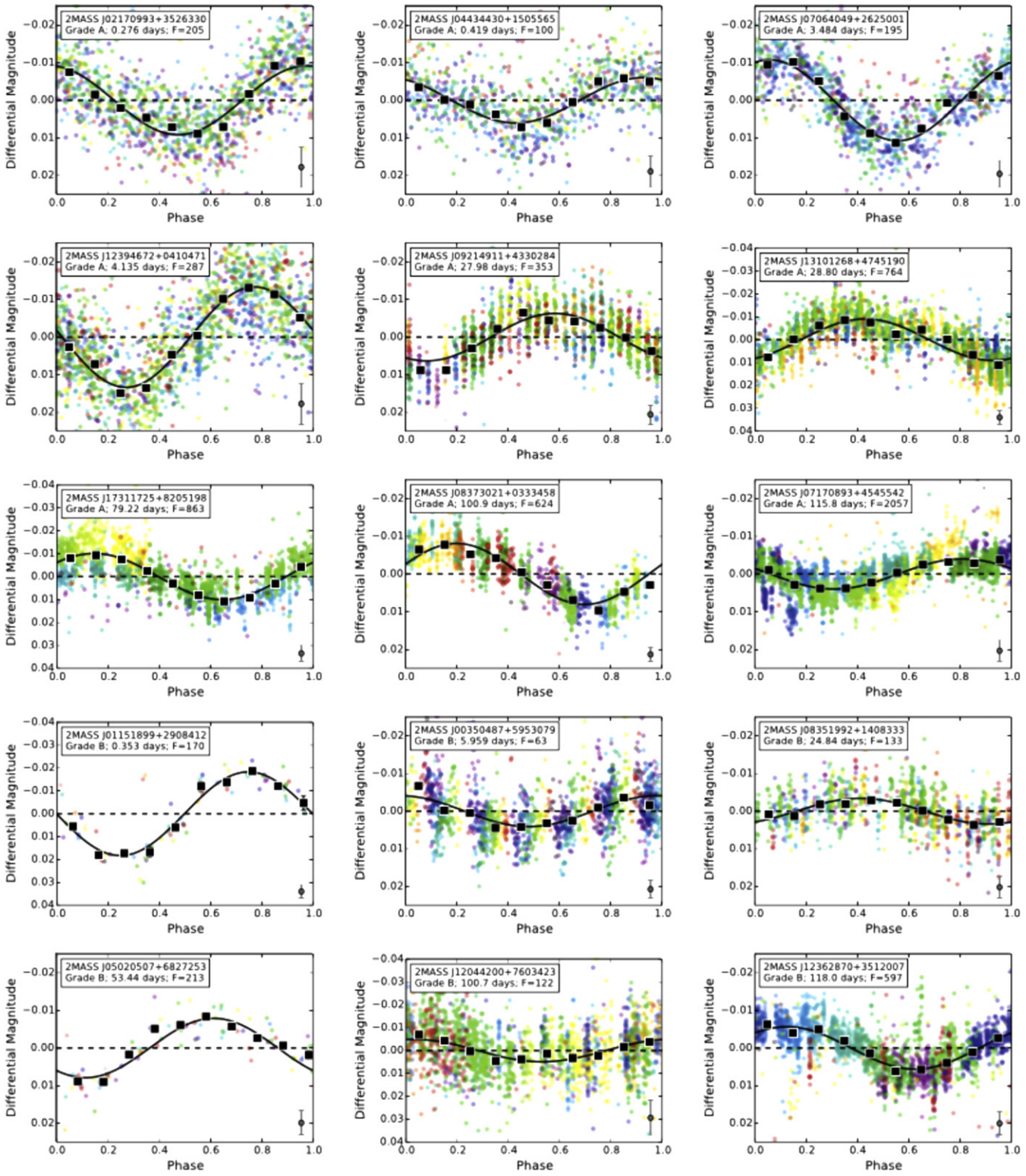

Figure 1. Examples of typical rotators, randomly selected from our sample. The top three rows show grade A rotators, and the bottom two rows show grade B rotators. Data points are colored according to the observation number, and the median error is indicated in the bottom right corner. The earliest data points are purple, the latest are red. We also show the median magnitude in ten uniformly spaced bins in phase; the sample scatter about the median is plotted but typically smaller than the plotting symbol. The label indicates the rating (grade A or B), the rotation period, and the F-test statistic (F). Phase-folded light curves for all 626 grade A and B rotators and for candidate detections are included as supplementary material in the online version of this article.

(The complete figure set (626 images) is available.)

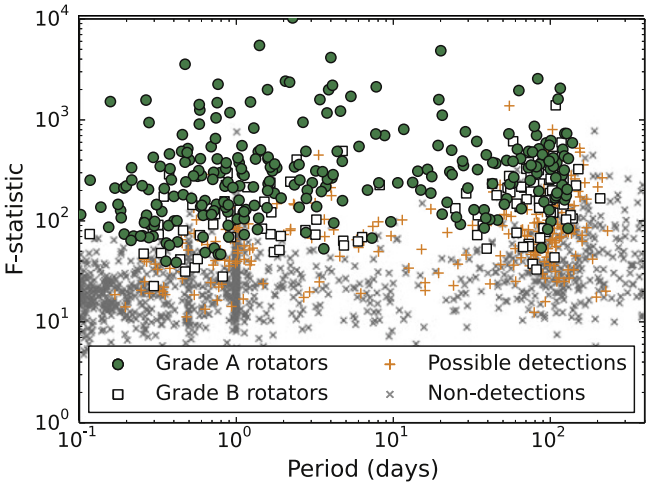

Figure 2. *F*-test statistic as a function of rotation period for grade A (filled circles) and grade B (open squares) rotators, "possible" detections (plus symbols), and non-detections (crosses).

periodogram peak) because there are usually multiple peaks in the periodogram, and an estimate based only on the dispersion about one particular peak would be misleading. We refer the reader to Irwin et al. (2011) for details of signal injection and recovery tests that can be used to gauge approximate period errors.

We include estimates of stellar mass and radius in Table 1. Only a portion of the table is shown here. Additional columns, including rotation period and mass, are included in the machine-readable table. Our stellar masses are estimated from the absolute K magnitude, using the relation from Delfosse et al. (2000), which we modified to allow extrapolation past the limits of the calibration. The relation is unphysical beyond the calibration range of $4.5 < M_K < 9.5$, and a number of our stars are fainter than this limit. Our modification simply enforces a constant value and first-derivative slope at the boundaries, and produces a physically reasonable result. For stellar radii, we use the mass–radius relation from Boyajian et al. (2012).

We also include non-rotators with "possible" or "no detection" ratings in Table 1, listing the period of the strongest peak in the periodogram. We caution that these periods should not be interpreted as detections. Additional data would be useful for confirming or disproving the listed periods.

The rotation periods and ratings in this paper supersede those reported previously in Irwin et al. (2011) and West et al. (2015).

3.2. Identifying Multiples

The multiplicity fraction among mid M dwarfs is around 30% (see, e.g., Winters 2015 for a review). Close companions can affect a star's rotation through tidal synchronization or disruption of the protostellar disk (e.g., Meibom & Mathieu 2005; Morgan et al. 2012). Unresolved multiples or background objects could also result in spurious period detections. Our tables note objects identified as multiples in the literature or by visual inspection, and any objects where the MEarth photometric aperture contained known background sources. Including both bright and faint companions, 228 objects in our sample have a nearby, physically associated companion and 448 have a source in the background. We additionally note objects identified as potentially overluminous in our previous work. These were identified by Newton et al. (2015), on the basis of their absolute magnitudes and spectroscopically derived luminosities, or by Dittmann et al. (2016), using their absolute magnitudes and colors.

The analysis in this paper excludes 449 objects that have bright, unresolved companions (regardless of whether they have common proper motion or are background objects, contamination flag 1), or have been identified as overluminous (flag 4). This excludes 211 of the 230 objects with a nearby, physically associated companion (12% of the full sample). The contaminants are distributed proportionally across the four possible period detection ratings. Objects with faint companions are not excluded.

2MASS J11470543+7001588 (G 236-81) is one such multiple, and is the only object in which we clearly detect two unrelated periods. The periods are 3.49 and 5.37 days.

3.3. Defining a Statistical Sample

For questions that seek to address how the rotators are different from the non-rotators, we need to know whether or not we could have detected rotation with a certain period and amplitude in a given star. The full Monte Carlo simulation necessary to adequately address period recovery is computationally intensive, so we instead use global properties of the light curves to define a "statistical sample" of stars for which we believe we could have detected long rotation periods. We find that a combination of the number of visits ($n_{\rm visits}$) to an object and the typical error (σ) of each visit is strongly predictive of whether or not we detected a rotation period, leading us to define the statistical sample as all stars with $n_{\rm visits} > 1200$ and $\sigma < 0.005$ mag, where σ is the median theoretical error divided by the square root of the number of exposures per visit. There are 311 stars in the statistical sample.

We show the distribution of periods in the statistical sample in Figure 3. The grade A rotators are biased toward shorter periods, which are easier to positively identify as being the result of stellar variability even within the statistical sample. The primary reason is that a short-period rotator undergoes more rotation cycles in a given amount of time than does a long-period rotator. The multiple rotation cycles seen for short periods help to confirm low-amplitude signals in noisy data, and cause a greater fraction of stars to have enough data to satisfy our requirement of two cycles of modulation (see Section 3.1). The tendency for the grade B rotators and candidate rotators to have long periods is therefore due to the incompleteness of grade A rotators at long periods. Non-detections favor non-astrophysical periods that are near 1 day or very long (1000 days).

We see a relative lack of stars with intermediate rotation periods around 30 days, which we suggest is astrophysical in origin. In the statistical sample, the distribution of best-fitting periods for all stars (including possible detections and stars with no detection) does not indicate a large population of intermediate rotators. This lends support to the idea that our classification by eye is not lacking sensitivity to intermediate-period rotators.

4. COMPARISON TO PREVIOUS PERIOD MEASUREMENTS

A few dozen of our stars have been the targets of other surveys. In this section, we take a closer look at these objects.

Table 1
Kinematics and Rotation Periods for All Rotators and Non-rotators

2MASS ID	R.A. (deg)	Decl. (deg)	π (arcsec)	$PM_{R.A.}$ (arcsec/yr)	$PM_{Decl.}$ (arcsec/yr)	v_{rad} (km s^{-1})	U (km s^{-1})	V (km s^{-1})	W (km s^{-1})
Grade A rotators									
J00011579+0659355	0.315872	6.99324	0.0571	−0.4504	−0.0810	−1.0	35.7	11.4	4.2
J00151880+4344347	3.82845	43.743	0.0351	0.3211	0.0380	4.0	−30.2	−10.4	−0.8
J00165678+2003551	4.23668	20.0653	…	0.2427	0.0240	4.0	…	…	…
J00185352+2748499	4.72329	27.8138	0.0692	0.4376	−0.1010	2.0	−21.1	−14.4	−10.1
J00240376+2626299	6.01583	26.4416	0.0453	0.1809	−0.0550	20.0	−19.4	3.5	−18.2

(This table is available in its entirety in machine-readable form.)

We first compare our work to that of other ground-based photometric surveys (Section 4.1). In Section 4.2, we look at the few MEarth objects with photometry from the *Kepler* space telescope. The rotational broadening of spectral features provides another means to determine stellar rotation, and we present a comparison to those studies in Section 4.3.

4.1. Comparison to Ground-based Photometry

We compare our grade A and B rotators to those with photometric periods from the literature. We additionally show objects with "possible" ratings. Including known multiples, we have overlap with Alekseev & Bondar (1998, 1 star in common), Norton et al. (2007, 5 stars), Hartman et al. (2010, 3 stars), Shkolnik et al. (2010, 2 stars), and Hartman et al. (2011, 25 stars). These values are presented in Table 2.

Hartman et al. (2011), our primary source for literature measurements, used data from HATNet that spanned time baselines of 45 days to 2.5 years. They searched for rotation periods between 0.1 and 100 days among all field K and M dwarfs using analysis of variance (AoV), which tries to find the period that minimizes the scatter in the phased light curve. They decorrelate against external parameters ("EPD" light curves), then against templates built from other objects in the field ("TFA" light curves), and report a quality flag for each detection. We exclude quality flags of 2, and by default use the TFA-based detections. We adopt the EPD-based detections if they have a better quality flag. We noticed that for 2MASS J17195298+2630026 (Gl 669 B), the two algorithms resulted in different periods. The TFA analysis gives $P = 1.45$ days, which agrees with the period we detect. The EPD analysis gives $P = 20$ days, the same period as both we and Hartman et al. (2011) determine for the common-proper-motion companion 2MASS J17195422+2630030 (Gl 669 A). Although the EPD period had the higher quality flag, we adopt the TFA period for this object.

We find excellent agreement between the periods measured from these surveys and the periods we measure from MEarth (Figure 4). Three objects are discrepant. For grade A rotator 2MASS J13505181+3644168 (LHS 6261), our period is 55.7 days while that from Hartman et al. (2011) is 72.2 days. We also detect a second strong frequency in this object with a period of 93 days. Our frequencies evenly bracket the detection of Hartman et al., so we suspect our periodogram peak has been split as a result of the window function of the MEarth data. For our "possible"-rated object 2MASS J14545496+4108480 (LP 222-15), we find a period of 0.858 days, while Hartman et al. (2011) measure a period of 6.11 days. There is a peak in our periodogram at 6.2 days, and 0.858 is close to the one-day sampling alias of this signal. For our "possible"-rated object 2MASS J13314666+2916368 (DG CVn), we measure $P = 0.268$ days, while Robb et al. (1999) measure 0.108 days. Our candidate signal is affected by both the sparse data set and the changes in baseline magnitude.

4.2. Comparison to Kepler

The *Kepler* space telescope gathered multi-year photometry on approximately 150000 stars, including several thousand M dwarfs, most of which are early M dwarfs (Borucki et al. 2010; Koch et al. 2010). We downloaded *Kepler* light curves for the objects with simultaneous data from MEarth from the Mikulski Archive for Space Telescopes (MAST). We use the PDCSAP_FLUX data; this reduction was intended to remove instrumental systematics while retaining astrophysical variability (Smith et al. 2012; Stumpe et al. 2012). Ten targets in our sample also have data from *Kepler*. We examine the two that have periodic modulations in the *Kepler* data that are detectable by eye (Figure 5). We have not detected periods in the remaining objects, though we note that for KIC 6117602, we have a candidate detection of 80 days, which is at odds with the 0.67 day period reported by Rappaport et al. (2014).

For KIC 9726699 (GJ 1243, Figure 5, top panel), we detect a period at 0.59 days, which we assigned grade A. The period, including the indications of asymmetry, is easily identifiable in *Kepler* photometry. For KIC 9201463 (Figure 5, bottom panel), for which the *Kepler* light curve has a clear 5.5 day signal, we did not detect a rotation period in the MEarth data alone. However, the MEarth data have power at this frequency, and the modulation matches the phase of the *Kepler* signal. The MEarth bandpass is redder than that of *Kepler*, so we expect the amplitude to be lower in our data. The relatively small amplitude (0.5% in the *Kepler* bandpass), somewhat non-sinusoidal modulation, and the frequent flaring are also likely to contribute to our inability to detect the signal independently in MEarth.

4.3. Comparison to $v \sin i$ Measurements

The rate at which a star spins can also be inferred by measuring the broadening of spectral features due to the rotational velocity (v) of its photosphere. Due to the unknown inclination i, only $v \sin i$ can usually be determined. We searched the literature for previous measurements of $v \sin i$ for M dwarfs in the sample of Nutzman & Charbonneau (2008). The papers in which we looked for matches are listed in Table 3. We first compare $v \sin i$ measurements directly to other $v \sin i$ measurements from the literature (Section 4.3.1), and use

Table 2
Objects with Ground-based Photometric Periods from the Literature

2MASS ID	Grade[a]	MEarth P (days)	Lit. P (days)	References[b]
Rotators				
J00285391+5022330	A	1.093	1.09332	H11
J02024428+1334335	A	4.003	4.01	S10
J03223165+2858291	A	1.929	1.92673	H11
J03364083+0329194	A	0.328	0.32766	K12
J03425325+2326495	A	0.834	0.834379	H10
J07382951+2400088	A	3.875	3.87463	H11
J07444018+0333089	A	2.775	2.8	A98
J08065532+4217333	A	8.804	8.80699	H11
J09214911+4330284	A	27.984	28.7811	H11
J09441580+4725546	A	4.395	4.40041	H11
J09591880+4350256	A	0.755	0.7554	H11
J10512059+3607255	A	3.782	3.77885	H11
J11031000+3639085	A	2.056	2.05692	H11
J11115176+3332111	A	7.785	7.77026	H11
J11474074+0015201	A	11.662	11.603	K12
J13505181+3644168	A	55.239	72.1768	H11
J15553178+3512028	A	3.542	3.52093	H11
J17195422+2630030	A	20.511	19.8077	N07
J17335314+1655129	A	0.266	0.2659	N07
J18130657+2601519	A	2.285	2.2838	N07
J19510930+4628598	A	0.593	0.592578	H11
J20103444+0632140	A	1.121	1.12	S10
J21322198+2433419	A	4.747	4.7358	N07
J22232904+3227334	A	0.854	0.854	M11
J23025250+4338157	A	0.348	0.347704	H11
J23050871+4517318	A	1.285	1.28447	H11
J00161455+1951385	B	4.798	4.7901	N07
J03284958+2629122	B	3.235	3.23062	H10
J04381255+2813001	B	0.670	0.335985	H11
J17195298+2630026	B	1.457	1.454184	H11[c]
J23545147+3831363	B	4.755	4.757	K13
Candidates				
J02253841+3732339	U	15.135	14.6016	H11
J03264495+1914402	U	0.454	0.454016	H10
J10235185+4353332	U	56.311	60.7517	H11
J10382981+4831449	U	3.178	3.17243	H11
J13314666+2916368	U	0.268	0.10835	R99
J13374043+4807542	U	0.558	0.55754	H11
J14545496+4108480	U	0.858	6.11491	H11
J14592508+3618321	U	4.173	4.16904	H11
J15040626+4858538	U	1.022	1.02136	H11
J15192126+3403431	U	2.211	2.21031	H11

Notes.
[a] MEarth period rating, see description in the text.
[b] Reference for literature photometric period. A98 = Alekseev & Bondar (1998), R99 = Robb et al. (1999), N07 = Norton et al. (2007), H10 = Hartman et al. (2010), S10 = Shkolnik et al. (2010), H11 = Hartman et al. (2011), M11 = Messina et al. (2011), K12 = Kiraga (2012), K13 = Kiraga & Stępień (2013).
[c] Period from TFA light curve, see the text for discussion.

lessons from this analysis in our comparison of $v \sin i$ and photometric rotation period (Section 4.3.2).

4.3.1. Comparison Between v sin i Measurements in the Literature

Several of the surveys with $v \sin i$ measurements for our targets used spectrographs with resolving powers ($R \equiv \lambda/\Delta\lambda$) of 20,000 to 40,000. At these resolutions, the rotational broadening of all but the most rapid rotators falls below the resolution of the spectrograph, and disentangling non-astrophysical sources of broadening from rotational broadening is challenging.

We directly compare $v \sin i$ for M dwarfs from different literature sources, regardless of whether the star was observed by MEarth, in Figure 6. Since we do not know the true $v \sin i$, we adopt the value measured by the survey with the highest spectral resolution (which we call the "primary" survey) and compare it to values measured by surveys with lower spectral resolution ("secondary" surveys). We require that the resolution of the primary survey be greater than 40,000.

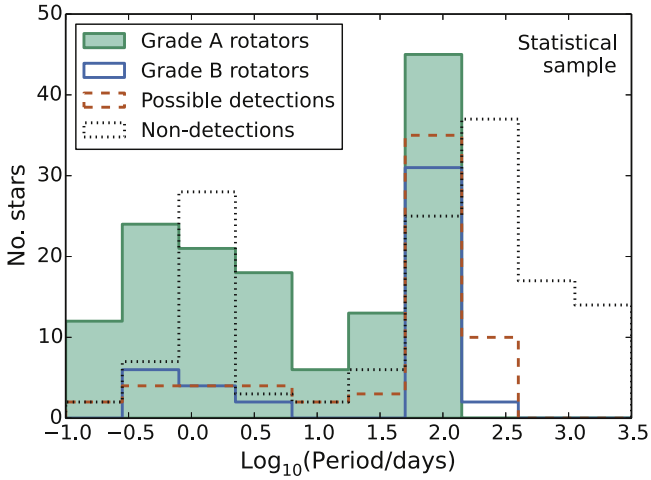

Figure 3. Distribution of best-fitting periods for the grade A and grade B rotators, and uncertain detections in our statistical sample. The lack of grade A rotators at long periods is likely a result of incompleteness. We see a relative lack of stars with intermediate rotation periods, which we suggest is astrophysical in origin.

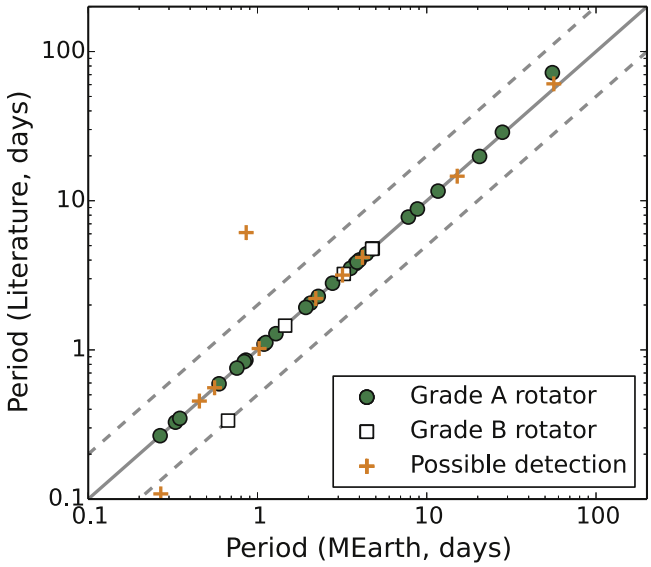

Figure 4. Comparison between photometric period measurements from this work (horizontal axis) and literature sources (vertical axis). We indicate the MEarth period rating assigned for each star with different symbols: grade A rotators (filled green circles), grade B rotators (open green pentagons), and possible detections (orange pluses). The solid line indicates exact agreement, while the dashed lines indicate periods twice or half of what we measure. The strong outlier with a literature period at 6.11 days likely results from the daily sampling alias.

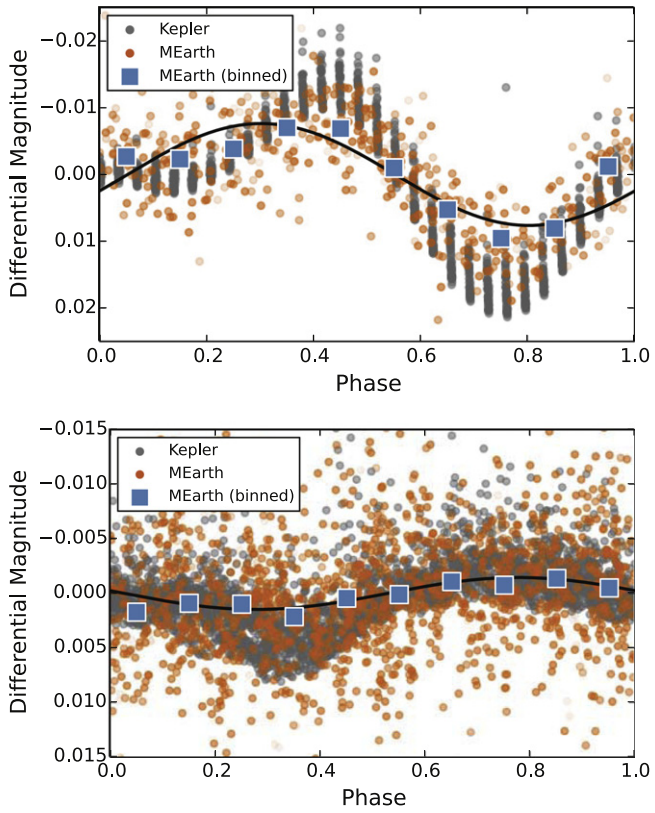

Figure 5. Phased light curves for objects in common between the MEarth and *Kepler* samples, for which a rotation period was detectable by eye in *Kepler*. For KIC 9726699 (top), the rotation period is the best-fitting one found by our analysis. For KIC 9201463 (bottom), the period was identified first in the *Kepler* light curve, after which we found the closest-fitting peak in the periodogram of the MEarth data. Gray points show a subset of the *Kepler* data, MEarth data from the same period of time are shown in orange (with increasing transparency indicating data with larger errors), and the binned MEarth data in blue. The black curve is the sinusoid that best fits the MEarth data.

For $v \sin i > 20\,\mathrm{km\,s^{-1}}$, the primary and secondary surveys do not deviate systematically, but there are significant discrepancies for smaller values of $v \sin i$. We find that when inferring $v \sin i$ broadening that is below the spectral resolution, the secondary surveys tend to determine higher values for $v \sin i$ than the primary survey, and the magnitude of the discrepancy varies with the significance of the reported detection. Here we define the $v \sin i$ significance as the $v \sin i$ measured by the primary survey divided by the resolving power in $\mathrm{km\,s^{-1}}$ of the spectrograph used in the secondary survey. We find discrepancies in many $v \sin i$ detections with significances less than about 0.8. We therefore arrive at a similar conclusion to Reiners et al. (2012a), who found evidence that some detections of $v \sin i$ are spurious.[4] Improved treatment of $v \sin i$ detection limits, as well as additional or repeated $v \sin i$ measurements at higher resolving power, would be beneficial.

4.3.2. Comparison Between v *sin* i *and Photometric Measurements*

We compare the equatorial rotational velocities (v_{eq}) we infer from the photometric rotation period to the measured $v \sin i$ in Figure 7 and Table 4. This comparison includes our grade A and B rotators. v_{eq} is calculated from the estimated stellar radius (R) and the rotation period (P) using

$$v_{\mathrm{eq}} = \frac{2\pi R}{P}. \quad (4)$$

We do not calculate errors on the rotation period, so for this comparison we assume a 10% error on period (Irwin et al. 2011) and a 10% error on stellar radius (Delfosse et al. 2000; Boyajian et al. 2012). If the photometric rotation period, stellar radius, and the $v \sin i$ are correct, $v_{\mathrm{eq}} > v \sin i$. Significance is defined as before: the reported $v \sin i$ measurement divided by the resolving power of the spectrograph used.

We first note the stars with reported $v \sin i$ detections at low significance, for which the $v \sin i$ broadening is less than the resolving power of the spectrograph used (brown circles and squares in Figure 7). These include the three objects for which

Table 3
Sources for $v \sin i$ Compilation

Abbreviation	Reference	Resolving Power (R/1000)
V83	Vogt et al. (1983)	115
SH86	Stauffer & Hartmann (1986)	20
S87	Stauffer et al. (1987)	20
MC92	Marcy & Chen (1992)	40
T92	Tokovinin (1992)	18
JV96	Johns-Krull & Valenti (1996)	120
S97	Stauffer et al. (1997)	44
D98	Delfosse et al. (1998)	42
TR98	Tinney & Reid (1998)	19
B00	Basri et al. (2000)	31
S01	Schweitzer et al. (2001)	34/45
G02	Gizis et al. (2002)	19
R02	Reid et al. (2002)	33
MB03	Mohanty & Basri (2003)	31
B04	Bailer-Jones (2004)	39
FS04	Fuhrmeister & Schmitt (2004)	45
J05	Jones et al. (2005)	42
Z05	Zickgraf et al. (2005)	20/22/34
T06	Torres et al. (2006)	50
Z06	Zapatero Osorio et al. (2006)	20
R07	Reiners & Basri (2007)	200
RB07	Reiners & Basri (2007)	31
H07	Houdebine (2008)	45
RB08	Reiners & Basri (2008)	31/33
J09	Jenkins et al. (2009)	37
WB09	West & Basri (2009)	31
B10	Blake et al. (2010)	25
H10	Houdebine (2010)	40/42/75
RB10	Reiners & Basri (2010)	31/32
B10	Browning et al. (2010)	60
R12	Reiners et al. (2012a)	40/48
Bai12	Bailey et al. (2012)	30
Bar12	Barnes et al. (2012)	35
D12	Deshpande et al. (2012)	20
H12	Houdebine (2012)	75/115
K12	Konopacky et al. (2012)	30
T12	Tanner et al. (2012)	24
D13	Deshpande et al. (2013)	22.5
M13	Mamajek et al. (2013)	100
B14	Barnes et al. (2014)	54
M14	Malo et al. (2014)	50/52/68/80
D15	Davison et al. (2015)	57
HM15	Houdebine & Mullan (2015)	75/115

[4] Houdebine & Mullan (2015) carried out a comparison of $v \sin i$ values and found that their measurements and other surveys agreed well. However, their comparison did not include all of the lower-resolution surveys we considered.

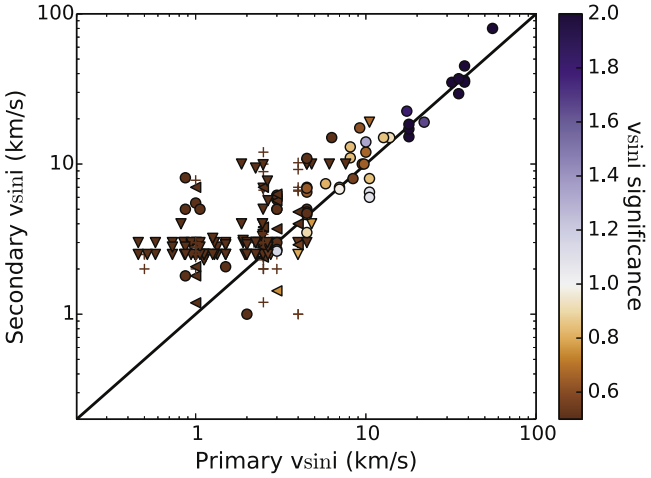

Figure 6. Comparison of $v \sin i$ measurements from the literature for M dwarfs in our database. The horizontal axis shows the $v \sin i$ measured by the survey with the highest spectral resolution (requiring $R > 40{,}000$, called the "primary" survey), while the vertical axis shows the $v \sin i$ measured from other ("secondary") surveys. The color indicates our estimate of the significance of the detection; smaller values (brown) are less significant, while larger values (purple) are more so. The symbol shape indicates whether the reported value is a detection or an upper limit: solid circles indicate detections reported by both the primary and secondary surveys; triangles pointed downwards indicate that the secondary survey reported an upper limit; triangles pointed toward the left indicate that the primary survey reported an upper limit; plus symbols indicate that both the primary and secondary surveys report upper limits.

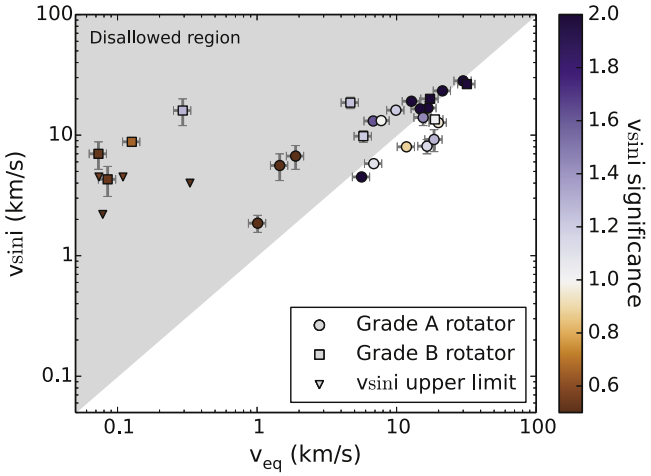

Figure 7. Comparison of estimated equatorial rotation velocities (horizontal axis) and $v \sin i$ measurements from the literature. The color indicates our estimate of the significance of the detection, assuming the $v \sin i$ reported and the resolution of the spectrograph used; smaller values (brown) are less significant, while larger values (purple) are more so. Solid circles (for grade A rotators) and squares (for grade B rotators) indicate $v \sin i$ detections, while triangles indicate an upper limit. Errors on $v \sin i$ are included where available, and we have estimated errors for $v_{\rm eq}$. The gray shaded region indicates the region where $v \sin i > v_{\rm eq}$; no detections should fall in this region.

we measured long photometric rotation periods but that have $v \sin i$ measurements indicating rapid rotation. Based on the analysis we presented previously in Figure 6, these low-significance $v \sin i$ detections may be incorrect, and we suggest that this is the cause of the disagreement with our results.

We will now consider only $v \sin i$ detections at higher significance (white and purple points in Figure 7). Our photometric periods concur with the detection of rapid spin from rotational broadening. However, $v \sin i$ still exceeds $v_{\rm eq}$ in some cases, so one or more of the $v \sin i$, our photometric period, or the radius estimate must be in error. In some cases, the highest peak in the periodogram may represent an alias or harmonic of the true period of the star. The most extreme example is 2MASS J23134727+2117294 (LP 462-11), with $v \sin i = 16\ {\rm km\ s^{-1}}$ and $P = 34.5$ days ($v_{\rm eq} = 0.3\ {\rm km\ s^{-1}}$). Our light curve for this object is relatively sparse (which engendered it a grade B rating); and although the strongest signal in the periodogram is at $P = 34.5$ days, a rotation period of close to one day also provides a reasonable fit to the data. Table 5 considers stars with $v \sin i > v_{\rm eq}$ and provides the strongest signal at periods shorter than the best-fitting period.

5. SPOT CHARACTERISTICS

We consider different aspects of starspots in this section. First, we investigate the relationship between semi-amplitude and rotation period (Section 5.1), then consider spot patterns and the stability of the photometric modulations (Section 5.2). In Section 5.3, we compare the fraction of stars that we detect to be rotating with the recovery rates of photometric and $v \sin i$ surveys.

5.1. Amplitude of Variability

The amplitude of the photometric modulation is derived from the combined effect of the contrast between the spotted and unspotted stellar photosphere and the longitudinal inhomogeneity in the distribution of spots. Starspots, in turn, are surface manifestations of a star's magnetic field. Because rotation, magnetic fields, and starspots are closely related, we might therefore expect a correlation between rotation period and amplitude.

Hartman et al. (2011) found that the rotation periods and amplitudes of K and early- to mid-M dwarfs are uncorrelated for periods less than 30 days (see Figure 16 in their work), and that amplitude decreases with increasing rotation period for $P > 30$ days. For later M dwarfs, Hartman et al. (2011) similarly found no correlation between amplitude and period for periods of up to 30 days, but their sample contained few objects at longer periods. An anticorrelation was also seen by McQuillan et al. (2014) for M dwarfs in the *Kepler* sample; this sample is dominated by early M dwarfs and considered all stars with $T_{\rm eff} < 4000$ K together. McQuillan et al. (2014) also identified a population of rotators with periods <15 days and high variability at a range of effective temperatures; examining Figure 14 in their work, the amplitude and period for this population appear uncorrelated. They postulate that these objects are binaries.

We use semi-amplitudes in this analysis, where the semi-amplitude is defined as the coefficient of the best-fitting sinusoid (a in Equation (2)). Data on a single star may include several light curves whose semi-amplitudes are fit independently; the values we use are those from the light curve with the most observations. We derive errors using the covariance matrix from our least-squares fit, which does not include uncertainty in the period (see Section 3). The median amplitude error is 0.002 mag, and is independent of rotation period and the rating we have assigned for the period. Note that if the light curve is evolving or shows non-sinusoidal behavior, the semi-amplitude is suppressed relative to the peak-to-peak amplitude.

In Figure 8, we plot the semi-amplitude of variability versus rotation period for higher-mass ($0.25 < M \lesssim 0.5\ M_{\odot}$) and

Table 4
Rotators with $v \sin i$ Measurements

2MASS ID	Grade	MEarth P[a] (days)	v_{eq}[b] (km s^{-1})	$v \sin i$ (km s^{-1})	Resolving Power (R/1000)	References[d]
J02170993+3526330	A	0.3	30.0 ± 4.2	28.2 ± 0.7	37	J09
J02204625+0258375	A	0.5	21.3 ± 3.0	23.3 ± 0.7	37	J09
J03205965+1854233	A	0.6	11.8 ± 1.7	8.0 ± ⋯	33	R02
J03425325+2326495	A	0.8	19.9 ± 2.8	12.7 ± 0.5	22.5	D13
J06000351+0242236	A	1.8	6.9 ± 1.0	5.8 ± 0.3	57	D15
J07444018+0333089	A	2.8	5.6 ± 0.8	4.5 ± ⋯	200	R07
J08294949+2646348	A	0.5	16.5 ± 2.3	8.1 ± 1.1	42	D98
J08505062+5253462	A	1.8	6.8 ± 1.0	13.1 ± 0.7	37	J09
J09301445+2630250	A	10.7	1.9 ± 0.3	6.7 ± 1.5	22.5	D13
J09535523+2056460	A	0.6	14.8 ± 2.1	16.5 ± 0.4	37	J09
J10163470+2751497	A	22.0	0.33 ± 0.05	<4.0	33	R02
J10521423+0555098	A	0.7	12.8 ± 1.8	19.1 ± 0.2	37	J09
J11474074+0015201	A	11.7	1.5 ± 0.2	5.6 ± 1.4	22.5	D13
J12185939+1107338	A	0.5	18.6 ± 2.6	9.2 ± 1.9	42	D98
J13003350+0541081	A	0.6	16.8 ± 2.4	16.8 ± 2.1	42	D98
J13564148+4342587	A	0.5	15.5 ± 2.2	14.0 ± 2.0	31	R10
J17195422+2630030	A	20.5	1.0 ± 0.1	1.9 ± 0.3	75	H12
J18024624+3731048	A	123.8	0.07 ± 0.01	<4.5	37	J09
J18452147+0711584	A	0.8	9.9 ± 1.4	16.1 ± 0.1	22.5	D13
J19173151+2833147	A	1.1	7.8 ± 1.1	13.2 ± 0.5	22.5	D13
J22245593+5200190	A	81.8	0.11 ± 0.02	<4.5	37	J09
J03132299+0446293	B	126.2	0.08 ± 0.01	<2.2	42	D98
J05011802+2237015	B	70.7	0.13 ± 0.02	8.8 ± 0.3	22.5	D13
J06022918+4951561	B	104.6	0.08 ± 0.01	4.3 ± 1.2	37	J09
J09002359+2150054	B	0.4	17.4 ± 2.5	20.0 ± 0.6	37	J09
J11005043+1204108	B	0.3	31.9 ± 4.5	26.5 ± 0.8	22.5	D13
J12265737+2700536	B	0.7	18.8 ± 2.7	13.5 ± 0.6	22.5	D13
J16370146+3535456	B	100.4	0.07 ± 0.01	7.0 ± 1.8	22.5	D13
J22081254+1036420	B	2.4	4.7 ± 0.7	18.6 ± 2.0	20	D12
J23134727+2117294	B	34.5	0.29 ± 0.04	16.0 ± 4.0	24	T12
J23354132+0611205	B	1.7	5.8 ± 0.8	9.8 ± 1.1	37	J09

Notes.
[a] Rotation period determined from MEarth photometry in this work.
[b] Equatorial rotation velocity and error calculated from the MEarth rotation period and the estimated stellar radius, assuming 10% errors on both the radius and the period.
[c] Resolving power of the spectrograph used in the $v \sin i$ study, divided by 1000.
[d] Reference code for $v \sin i$ measurement. See Table 3.

Table 5
Alternative Short-period Signals for Stars with $v \sin i > v_{eq}$

2MASS ID	Grade	MEarth P[a] (days)	v_{eq}[a] (km s^{-1})	F-stat	Alt. P[b] (days)	Alt. v_{eq} (km s^{-1})	Alt. F-stat	$v \sin i$ (km s^{-1})
J02204625+0258375	A	0.5	21.4	270	0.33	32.4	180	28.2
J08505062+5253462	A	1.8	6.8	250	0.64	19.1	140	13.1
J09301445+2630250	A	10.7	1.9	160	0.91	22.3	100	6.7
J09535523+2056460	A	0.6	14.8	75	0.38	23.4	60	16.5
J10521423+0555098	A	0.7	12.8	360	0.41	21.9	250	19.1
J11474074+0015201	A	11.7	1.5	540	1.09	16.1	340	5.6
J17195422+2630030	A	20.5	1.0	740	1.05	19.5	540	1.9
J18452147+0711584	A	0.8	9.9	150	0.46	17.2	110	16.1
J19173151+2833147	A	1.1	7.8	80	0.53	16.2	50	13.2
J22081254+1036420	B	2.4	4.7	180	0.7	16.1	180	18.6
J23134727+2117294	B	34.5	0.3	80	1.03	10.0	50	16.0
J23354132+0611205	B	1.7	5.8	40	0.62	15.9	30	9.8

Notes.
[a] Rotation period and v_{eq} determined from MEarth photometry, reproduced from Table 4 for clarity.
[b] Alternative periods with power in the MEarth data. These periods are less significant than the adopted period.

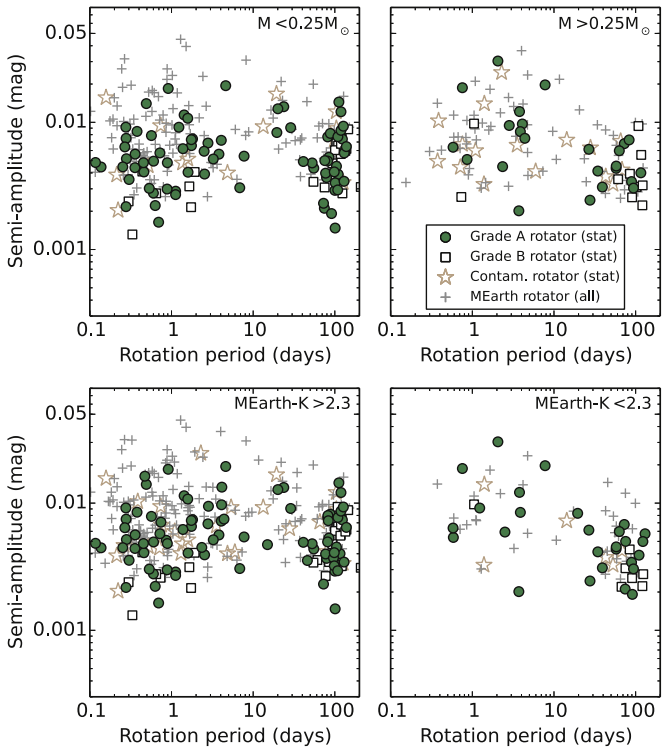

Figure 8. Semi-amplitude of variability (defined as the coefficient of the sinusoid in our best fit) vs. photometric rotation period, for $M < 0.25\,M_{\odot}$ (left panel) and $M > 0.25\,M_{\odot}$ (right panel). The median error on semi-amplitude is 0.002 mag. We caution that due to our use of absolute magnitudes to estimate stellar mass, a greater proportion of objects assigned to the higher mass bin are likely to be unresolved multiples. For objects in our statistical sample, we plot the grade A rotators (filled circles) and B rotators (open squares), and rotators with unresolved companions or that appear overluminous (open stars). We also show, for reference, all rotators not in the statistical sample (plus signs). Our sensitivity to high-amplitude, short-period rotators in sparse data sets can be seen in the overabundance of these objects in our full sample.

lower-mass ($0.08 \lesssim M < 0.25\,M_{\odot}$) M dwarfs in MEarth. Our mass limits approximate the $V - K$ color limits used by Hartman et al. (2011). We show the divisions based on both stellar mass (estimated from absolute K magnitudes) and color (using $MEarth - K$). We use our statistical sample in this analysis to avoid bias because high-amplitude, rapid rotators can be detected in many light curves where our method is not sensitive to lower-amplitude or longer-period variables.

We find a negative correlation between period and semi-amplitude for the higher-mass M dwarfs, but no correlation for mid M dwarfs, consistent with previous results. We use a Spearman rank correlation analysis to test the statistical significance of these results, and calculate the p-value for a two-sided hypothesis test with the null hypothesis that the data are uncorrelated, using the SciPy `stats` package. Smaller p-values indicate higher confidence that the correlation is not due to chance. The correlation coefficient including both the grade A and B rotators is -0.43 ± 0.07 for $M > 0.25\,M_{\odot}$ ($p = 0.01$) and -0.01 ± 0.03 for $M < 0.25\,M_{\odot}$ ($p = 0.5$). Values reported are the median and 68% confidence limits from a Monte Carlo simulation where we resampled with perturbation as suggested by Curran (2014). The lack of correlation for the lower-mass stars also persists if we consider narrower ranges in mass.

5.2. Spot Patterns and Stability

In keeping with our finding of the lack of a correlation between rotation and semi-amplitude, we find that most of our detected rotators show phase-folded light curves with qualitatively similar morphologies. At the precision of our data, they are usually sinusoidal in appearance. This could imply that the photometric modulations are the result of many spots acting in concert, or of long-lived polar or high-latitude spots viewed at high inclination. Considering the former scenario, Jackson & Jeffries (2013) demonstrated that photometric modulations of the amplitude we see can be produced by a large number of randomly distributed spots. The latter scenario is reflected in the prevalence of poloidal, axisymmetric large-scale fields recovered by Zeeman Doppler imaging for fully convective stars (e.g., Morin et al. 2008), and in spot models from time series photometry or spectroscopy (e.g., Barnes et al. 2015; Davenport et al. 2015). These patterns tend to be stable over multiple rotation cycles, and in some cases over more than a year.

Aided by our visual inspections of the data, we are able to detect objects with evolving spot patterns. We highlight 2MASS J23254016+5308056 (LHS 543a) as the star demonstrating the strongest spot evolution in our sample. Light curves for this star, which we classify as a grade A rotator with a rotation period of 23.5 days, are shown in Figure 9. The patterns seem stable for about two rotation cycles, and show evolution over roughly 200 days. We stress, however, that we expect our period detection method to be less effective for stars on which the spot patterns evolve on timescales comparable to the stellar rotation period.

Zeeman Doppler imaging measurements of late M dwarfs indicate that the magnetic field topologies of these stars can be very different for stars with similar properties. Donati et al. (2008) found that some late M dwarfs had axisymmetric, mostly dipolar fields (similar to earlier M dwarfs), while some are weaker, with more energy at small scales. We do not see any obvious dichotomy among the patterns of variability, but it is possible that one of the magnetic field topologies is more effective at producing spot contrast than the other.

5.3. Recovery Fractions

Previous photometric surveys have found a high fraction of fully convective stars to be photometrically variable. McQuillan et al. (2014) find that approximately 80% of the latest M dwarfs in *Kepler* have periods detected from their autocorrelation analysis, noting that their recovery of periods for these stars is not limited by the amplitude of variability. The recovery fraction of ground-based surveys is usually lower due to the cadence and precision of the observations. Hartman et al. (2011), correcting for incompleteness using signal injection, estimate that 50% of the stars with $M \lesssim 0.2\,M_{\odot}$ are variable at semi-amplitudes $\gtrsim$0.005 mag in their bandpass (Cousins I_C and R_C).

Our recovery rate of grade A and B rotators in the statistical sample is (47 ± 5)%, with no significant difference between the low- and high-mass populations. Considering $P < 100$ days to match the period range studied by Hartman et al. (2011), our recovery rate is (36 ± 4)%. The amplitude sensitivity of the two surveys is similar, but HATnet uses bluer photometric bandpasses where the contrast between the stellar photosphere and cooler spots is higher. We have also not

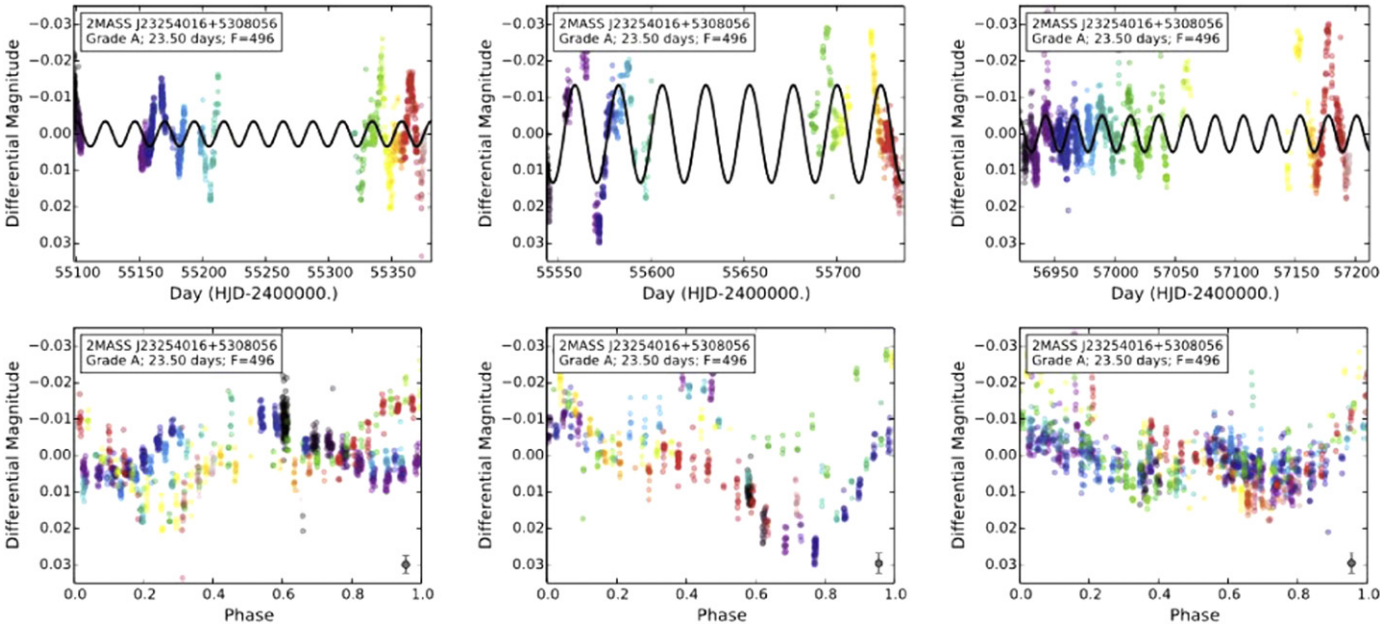

Figure 9. Light curves of 2MASS J23254016+5308056 (LHS 543a) from 2008 to 2010 (left), 2010 to 2011 (center), and 2011 to 2015 (right). The top panels show the brightness as a function of time, with the best-fitting sinusoidal model overplotted; the bottom panels show the light curves phase-folded to the best period. This object has the strongest and most rapid spot evolution of the stars in which we detect rotation periods. As in Figure 1, the color of the data points indicates the observation epoch. The median error is represented in the bottom corner.

modeled the incompleteness of our survey, though our use of the statistical sample mitigates the larger part of this effect for stars with $P < 100$ days.

Surveys of $v \sin i$ indicate that a larger fraction of fully convective stars are rotating rapidly than does our work. In a volume-limited survey, Delfosse et al. (1998) found that 50% of field mid-M dwarfs (roughly M4V–M5V) are rotating rapidly enough to have detectable $v \sin i$. Mohanty & Basri (2003), using new measurements and including those from Delfosse et al. (1998), similarly found that half of their mid-M dwarf population (M4V–M5.5V) had detectable $v \sin i$. In another survey, Browning et al. (2010) found that 30% of M4.5V–M6V stars had detectable $v \sin i$. For a 0.2 $R_\odot$ star and a detection limit of 3 km s^{-1} (typical for the two $v \sin i$ studies discussed here), this implies a period of less than 3.3 days. We find that only (18 ± 2)% of stars in our statistical sample are grade A or B rotators with $P < 3.3$ days.

The stellar samples selected by these surveys may not be comparable. For example, as the MEarth sample is selected by proper motion, we are missing a larger fraction of stars with lower tangential velocities. These kinematically cold stars are likely to be preferentially younger and therefore faster rotators (see Section 6.1). We estimate that our sample represents 85% to 90% of the kinematically unbiased sample (see Section 6.1). If we add an additional 15% of stars to our sample and assume that all are rotating at $P < 3.3$ days, we can increase the fraction of rapid rotators to 30%. This would bring our results into agreement with those from Browning et al. (2010), but would still fall below the fractions reported by Delfosse et al. (1998) and Mohanty & Basri (2003).

Our photometric survey could have missed a population of short-period rotators: first, we know from KIC 9201463 that we are not able to detect all short-period rotators. Second, our method for period detection is not sensitive to stars whose spots evolve on timescales comparable to the stellar rotation period. The roughly 30% of rapid rotators we would need to have missed could be a population of rapidly rotating stars with spot patterns that are not stable or that do not provide variability amplitudes high enough for us to detect. Aliasing of periods near 1 day could also contribute (see Section 4.3).

6. KINEMATICS AND METALLICITIES OF THE ROTATORS

To study kinematics, we require information on both the stars' positions and their motions through the Galaxy. As our targets were selected from a proper motion survey (Lépine & Shara 2005), all have measured proper motions. The majority of our targets also have parallaxes from MEarth astrometry measured by Dittmann et al. (2014), though we use more precise measurements from the literature if available. We also gather RVs from the literature, many of which come from Newton et al. (2014), in which we used $R \approx 2000$ near-infrared spectra to measure absolute RVs to 4 km s^{-1}. This survey targeted many of the MEarth rotators that had been identified by the time of observation, but the availability of RVs still limits the fraction of stars for which we have kinematic information.

With all six phase space dimensions, we then calculate the U (radial, positive is toward the Galactic center), V (azimuthal), and W (vertical) velocity components and their errors using an implementation of the method of Johnson & Soderblom (1987), updated to ICRS using the Galactic coordinate system defined in Perryman et al. (1997, vol. 1, part 1, Section 1.5.3). These velocities are measured relative to the barycenter of the solar system. When we consider velocities relative to the local standard of rest, we will denote these velocities using the subscript LSR. We use solar velocities from Schönrich et al. (2010), adopting $(U_{\odot \mathrm{LSR}}, V_{\odot \mathrm{LSR}}, W_{\odot \mathrm{LSR}}) = (11, 12, 7)$ km s^{-1}. The median error in each component is 3 km s^{-1}, with the error in radial velocity typically dominating.

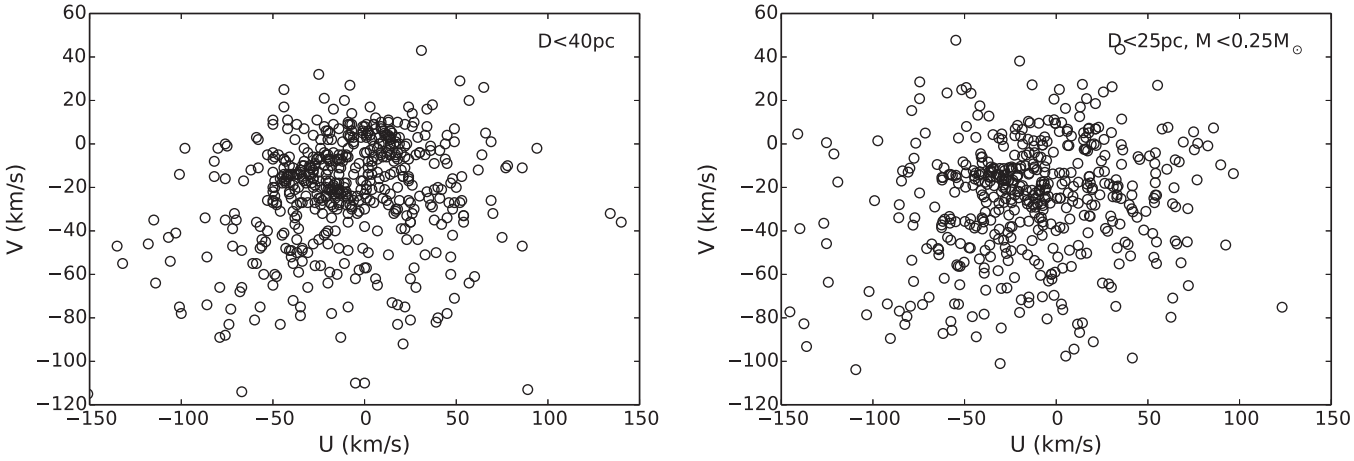

Figure 10. *U* and *V* velocities (relative to the Sun rather than the local standard of rest) for G and K dwarfs within 40 pc from the Geneva–Copenhagen Survey (GCS, left) and for mid-to-late M dwarfs within 25 pc from MEarth (right). The kinematic substructure evident in the GCS is also clearly seen in the nearby M dwarfs; most notable is the Hyades supercluster. The typical error on each component is 3 km s^{-1}.

6.1. De-biasing the Kinematics

The MEarth sample was selected from a proper motion survey with a lower limit of $0\farcs15$/yr, and therefore preferentially misses some stars with low tangential velocities. We simulate the stars that we missed due to proper motion limits by drawing velocities and distances from a model thin disk. We consider only the thin disk, because kinematically hotter stars are a small fraction of the solar neighborhood and less likely to be missed due to proper motion selection.

We draw $U_{\rm LSR}$, $V_{\rm LSR}$, and $W_{\rm LSR}$ from Gaussian distributions with standard deviations of 35 km s^{-1}, 20 km s^{-1}, and 16 km s^{-1}, respectively (Bensby et al. 2003). We draw distances and positions uniformly in volume. We also tested drawing from the observed distribution of the MEarth sample, and found little difference in the resulting simulated sample, consistent with the conclusions of Dittmann et al. (2014). We then compute proper motions and apply the selection criterion of $0\farcs15$/yr.

Out to a distance of 25 pc, we find that 11% of stars were missed due to the proper motion limits. Adding in the missing stars, the resulting velocity distributions for MEarth are similar to the distributions for volume-limited samples of more massive stars (e.g., Holmberg et al. 2009).

6.2. General Kinematic Properties of the Sample

In Figure 10 we show the *U* and *V* velocity components of the northern MEarth M dwarfs within 25 pc that have estimated masses less than 0.25 $M_\odot$. We place these limits to mitigate the likelihood of unresolved multiples contaminating the sample. We also show, for comparison, the G and K dwarfs from the Geneva–Copenhagen survey (GCS; Nordstrom et al. 2004; Holmberg et al. 2009) that are within 40 pc. The kinematic substructures that have been identified for higher-mass stars are clearly seen in our mid-to-late M dwarfs as well, most notably the arc at $U \approx -37$ km s^{-1}, $V \approx -17$ km s^{-1} that has been called the Hyades supercluster, the Hyades stream, and the Hyades moving group (Eggen 1958), not to be confused with the 625 Myr old Hyades open cluster.

The Hyades supercluster has similar kinematics to the Hyades and Pleiades open clusters, and at one time the supercluster was proposed to be a stream of stars evaporating from the Hyades open cluster, or at least composed of several coeval groups (Eggen 1992; Chereul et al. 1998, 1999) though this was not universally agreed upon (Dehnen 1998). However, recent theoretical work shows that spiral structure can dynamically create co-moving groups like the supercluster (De Simone et al. 2004; Quillen & Minchev 2005) and dynamical evolution is thought to be responsible for the larger kinematic structures in the solar neighborhood. For the Hyades supercluster, the dynamical origin of the kinematic association has been demonstrated observationally as well, through analysis of the chemical abundances and the mass function of stars in the proposed supercluster (Famaey et al. 2005, 2007, 2008; Bovy & Hogg 2010).

6.3. Disk Membership

Stars can be broadly grouped by their kinematics into the thin/young disk, the dynamically heated thick/old disk, and the even hotter halo population. We assign disk membership using the same method as Bensby et al. (2003), which takes into account the velocity dispersions in $U_{\rm LSR}$, $V_{\rm LSR}$, and $W_{\rm LSR}$ and the relative number densities of the different stellar populations. The values we use for the velocity dispersions of the thin disk, thick disk, and halo are also from Bensby et al. (2003). We assume that 89% of the stars in the solar neighborhood are in the thin disk, 10.6% in the thick disk, and 0.4% in the halo (Jurić et al. 2008). We do not consider membership in stellar streams.

In Figure 11, we plot the probability of an object being in the thick disk, *P*(thick), divided by the probability of that object being in the thin disk, *P*(thin), for the stars in the statistical sample. Out of 163 stars in the statistical sample that have *UVW* kinematic information, 23 ($14\% \pm 3\%$) have *P* (thick) > *P*(thin), and 7 have *P*(thick) > 10 × *P*(thin). Out of the 87 grade A and B rotators, 6 ($7\% \pm 3\%$) have kinematics that potentially place them in the thick/old disk, while none have *P*(thick) > 10 × *P*(thin). Overall, the rotators have kinematics typical of the solar neighborhood and are therefore generally members of the thin disk. Rapid rotators, however, are from a dynamically cold population. The *p*-value for a *k*-sample Anderson–Darling test (Scholz & Stephens 1987) to check whether the rotators are drawn from the field M dwarf population is $p = 10^{-5}$ for rotators with $P < 10$ days.

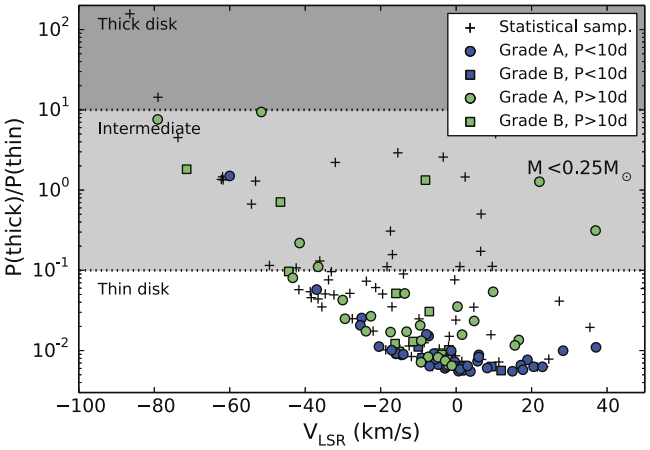

Figure 11. Probability (P) of an object being in the thick/old disk relative to the probability of it being in the thin/young disk, plotted against $V_{\rm LSR}$. $P_{\rm thick}/P_{\rm thin} = 1$ indicates an equal probability of the object being in either disk. Shaded regions denote disk assignments: $P > 10$ are thick/old disk members, $0.1 < P < 10$ are intermediate, and $P < 0.1$ are thin/young disk members. Only stars in our statistical sample are shown. Non-detections are plus symbols, grade A rotators are filled circles, and grade B rotators are filled squares. Blue indicates stars with periods shorter than 10 days, green those with periods longer than 10 days. Only stars in our statistical sample are shown.

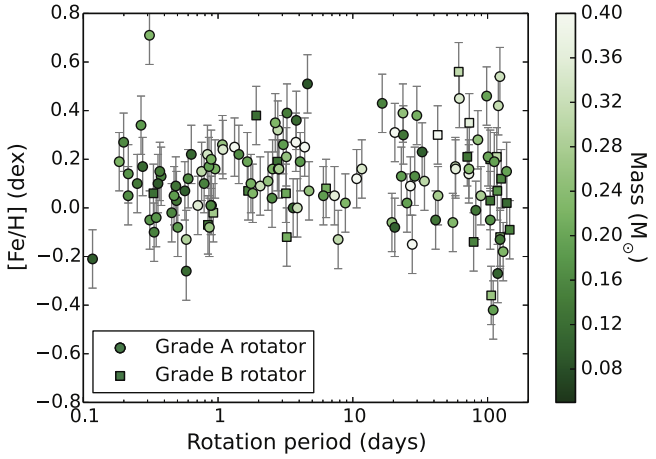

Figure 12. [Fe/H], estimated from near-infrared spectra, as a function of measured photometric rotation period. The typical error on [Fe/H] is 0.12 dex. The color of the points indicates their stellar mass as estimated from their absolute K magnitudes using our modified version of the relation of Delfosse et al. (2000). We do not see a clear trend between metallicity and rotation.

Our results differ from those of Irwin et al. (2011), who assigned approximately half of the MEarth rotators in their sample to the thick/old disk based on how closely the objects' kinematics matched those expected for each disk. This difference is primarily due to our inclusion of the thin–thick disk normalization.

The fraction of stars with detected periods depends on the kinematic subsample. We divide our statistical sample at $P(\text{thick}) = 0.1 \times P(\text{thin})$ to ensure enough stars in the kinematically older subsample. Our recovery fraction for kinematically young stars with $M < 0.25\,M_{\odot}$ is $(58 \pm 8)\%$, while for the kinematically old stars it is $(16 \pm 8)\%$. This may be the result of stars in the kinematically old subsample generally having longer periods, to which we believe our method is less sensitive (Section 5.3). Changing spot patterns or variability amplitude could also contribute, though we do not see any such trends among the sample of stars for which we do detect rotation periods.

6.4. Metallicities of the Rotators

Newton et al. (2014, 2015) estimated [Fe/H] for nearly 450 MEarth M dwarfs from near-infrared spectra. In Figure 12, we show [Fe/H] as a function of photometric rotation period. There is no clear trend with rotation, with a Spearman rank correlation of 0.00 ± 0.03 (see Section 5.1). This is consistent with the interpretation that the rotators are typical solar neighborhood stars: within the thin disk, there is no evidence for an age–metallicity relation, and stars may have a range of metallicities (e.g., Nordstrom et al. 2004).

The rotators do not appear significantly more metal-rich than the full sample (Anderson–Darling $p = 0.15^{+0.17}_{-0.09}$). We also do not see a correlation between metallicity and period (Spearman correlation coefficient $= -0.02^{+0.03}_{-0.02}$, $p = 0.5 \pm 0.2$), nor between metallicity and amplitude (coefficient $= 0.02^{+0.07}_{-0.08}$, $p = 0.5 \pm 0.2$).

There is one star with an unusually large (and unphysical) estimated metallicity of 0.7 dex: 2MASS J06052936+6049231 (LHS 1817). This star also has large U and W velocities. Two other rotators in our sample have estimated metallicities this high, and both were removed due to known or suspected multiplicity. All three of these objects were also identified as candidate young objects by Shkolnik et al. (2010), but are not the *only* stars in our sample that are potentially young. Although Shkolnik et al. (2010) have a high-resolution spectrum and did not identify 2MASS J06052936+6049231 as a multiple, its radial velocity ($>100\,\mathrm{km\,s^{-1}}$) makes it unusual in their sample as well.

7. THE AGE–ROTATION RELATION

Because low-mass main-sequence stars spin down with time, it is expected that slow rotators are older than their more rapidly rotating counterparts. While clusters can constrain the rotational evolution at young ages, there are no reliable methods to determine the ages of isolated field M dwarfs—once they reach the main sequence, their physical properties remain essentially unchanged over a Hubble time. As discussed in the introduction, galactic kinematics provide a means to probe the ages of groups of stars. For example, Irwin et al. (2011) used the total space velocities of 41 MEarth M dwarfs to classify the stars into the thin/young ($\lesssim$3 Gyr), intermediate (3–7 Gyr), and thick/old ($\gtrsim$7 Gyr) disks. Irwin et al. (2011) found that the young disk objects were entirely fast rotators, while the old disk objects were predominantly slow rotators.

We very clearly see the signatures of an age–rotation relation in the distribution of total space velocities as a function of photometric rotation period (Figure 13). There is an increase in dynamic hotness of the stellar population with rotation period, a trend that spans the entire period range that we probe. This is evidenced in the Spearman rank correlation coefficient for total space velocity and rotation period, which is 0.18 ± 0.03 ($p = 0.002^{+0.007}_{-0.002}$). We emphasize, however, that it is the velocity *dispersion* that increases with age. Stars with rotation periods of around a day have space velocities narrowly constrained, as would be expected for a very young stellar population. Stars with rotation periods around 100 days have a wide dispersion in space velocities, as expected for an older stellar population that has been dynamically heated.

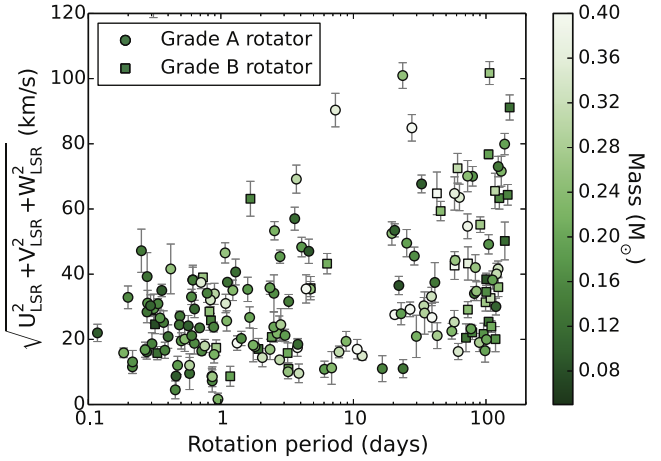

Figure 13. Total space velocity as a function of measured photometric rotation period. The color of the points indicates their stellar mass as estimated from their absolute K magnitudes using our modified version of the relation of Delfosse et al. (2000). The velocity dispersion increases with rotation period, as expected if the ages of stars are increasing with rotation period.

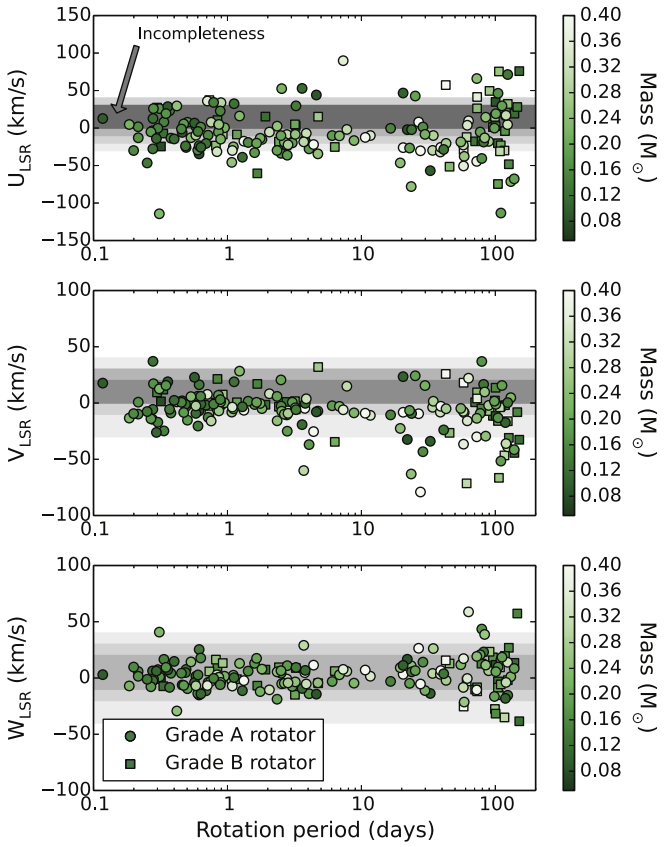

Figure 14. Individual components of space velocity as a function of measured photometric rotation period. The color of the points indicates their stellar mass as estimated from their absolute K magnitudes using our modified version of the relation of Delfosse et al. (2000). The velocity dispersion of each component increases with rotation period, as expected if the ages of stars are increasing with rotation period. The V component also becomes increasingly negative (asymmetric drift), which is also a sign of an older stellar population. The gray shaded regions show the percentage of stars that were missed in simulations as a result of our selection criteria. We show increments of 5%, up to 25%, e.g., the darkest gray band shows that at U velocities similar to the Sun, 25% of stars are missing from the MEarth sample. The darkest bands in V and W correspond to 20% and 15%, respectively.

Table 6
Velocity Dispersions and Ages for Stars with Detected Rotation Periods

Period Bin (days)	N stars	Mean P (days)	Mean W_{LSR} (km s^{-1})	σ_W (km s^{-1})	Est. Age (Gyr)
Grade A					
$0 < P < 1$	39	0.5	3	$6.0^{+1.8}_{-1.0}$	$0.5^{+0.4}_{-0.2}$
$1 < P < 10$	23	2.9	0	$7.4^{+1.8}_{-1.8}$	$0.7^{+0.5}_{-0.3}$
$10 < P < 70$	10	28.3	4	$6.5^{+1.6}_{-1.5}$	...
$P > 70$	14	102.4	9	$16.7^{+5.3}_{-4.5}$	$4.5^{+3.9}_{-2.3}$
Grade A+B					
$0 < P < 1$	43	0.5	3	$6.3^{+1.6}_{-1.3}$	$0.5^{+0.3}_{-0.2}$
$1 < P < 10$	31	2.9	1	$7.3^{+1.4}_{-1.4}$	$0.7^{+0.3}_{-0.3}$
$10 < P < 70$	11	29.9	5	$6.9^{+1.6}_{-1.8}$	...
$P > 70$	28	106.2	6	$17.7^{+5.4}_{-4.7}$	$5.1^{+4.2}_{-2.6}$

Decomposing the space velocities into the individual components (Figure 14), we see the same signatures of aging: the velocity dispersion of each component increases with rotation period. We also see evidence of asymmetric drift: the V velocities become more negative with increasing rotation period. As noted by West et al. (2015), the magnitude of asymmetric drift is much less than what is seen in more distant, older populations of M dwarfs.

The existence of a relationship between velocity dispersion and age among members of the thin disk is well established (e.g., Wielen 1977), though the exact form of the age–velocity relation is a matter of debate. Nordstrom et al. (2004) and Holmberg et al. (2009), using data from the GCS fit to a power law, find that velocity dispersion increases smoothly at least to 10 Gyr. In contrast, Soubiran et al. (2008) find an age–velocity relation with a shallower slope that saturates around 5 Gyr, using more distant clump giants. They also find significantly higher velocity dispersions, in contrast to studies of the solar neighborhood. Seabroke & Gilmore (2007) found that the data could not constrain whether the age–velocity relationship saturated beyond 5 Gyr using the data from Nordstrom et al. (2004).

Previous kinematic studies of low-mass stars have used the age–velocity relations of Wielen (1977)[5] (Schmidt et al. 2007; Faherty et al. 2009; Reiners & Basri 2009, 2010). We refer the reader to Reiners & Basri (2009) for comments on the usage of the equations. These studies relied on the total velocity dispersion. As discussed by Seabroke & Gilmore (2007), kinematic substructures such as the Hyades supercluster make the U and V velocity distributions non-Gaussian (see also Section 6.2). Therefore, we use the W velocity dispersion (σ_W) for kinematic age assignment.

In general, we find that the different functional forms and coefficients of age–velocity relations in the literature give consistent results for ages between 1 and 5 Gyr. The results diverge for older and younger populations. However, the age–velocity relationship is not appropriate for the youngest stars (as their kinematics are unrelaxed) and not well constrained at later ages (where it may saturate). Thus, the choice of age–velocity relation is not paramount. We adopt the results from Aumer & Binney (2009, see Table 6), who modeled the star

[5] Note that Ofek (2009) refit the original equations using data from Nordstrom et al. (2004).

formation history to arrive at the age–velocity relationship:

$$\sigma_W(\tau) = \sigma_{W,10}\left(\frac{\tau + \tau_1}{10\ \mathrm{Gyr} + \tau_1}\right)^{\beta}$$
$$\sigma_{W,10} = 23.8\ \mathrm{km\ s^{-1}}$$
$$\tau_1 = 0.001\ \mathrm{Gyr}$$
$$\beta = 0.445. \quad (5)$$

The velocity dispersion at 10 Gyr is described by the parameters $\sigma_{W,10}$ and τ_1, while the exponent β characterizes the heating rate.

To apply the age–velocity relation, we first need the dispersion of the W velocity component, σ_W. To determine the σ_W that underlies our data, we take the Bayesian approach of West et al. (2015), and maximize the posterior probability $p(\sigma_W|D)$, where our data D are our measurements of W_{LSR}. Using Bayes' theorem, the posterior probability is the product of the likelihood, $p(D|\sigma_W)$, and the prior, $p(\sigma_W)$:

$$p(\sigma_W|D) \propto p(D|\sigma_W) \times p(\sigma_W). \quad (6)$$

We use a Jeffreys prior, which is appropriate as an uninformative prior: $p(\sigma_W) \propto 1/\sigma_W$. The likelihood is the product of the probabilities of obtaining each measurement given the model. The underlying model to which we fit our data is a Gaussian distribution $\mathcal{N}(\mu_W, \sigma_W)$. We use a Cauchy distribution $\mathcal{C}(d_i, \sigma_i)$ to represent our measurement errors. The latter is centered at the measured value and has a standard deviation given by the error (σ_i) on each datum (d_i). This gives

$$p(D|\sigma_W) = \prod_i V(d_i - \mu_W; \sigma_W, \sigma_i) \quad (7)$$

where $V(W; \sigma_W, \sigma_i)$ is the probability density function (PDF) of a zero-mean Voigt profile, and can be written as the convolution of the PDFs of the Gaussian and Cauchy distributions $N(W; \mu, \sigma)$ and $C(W; \mu, \sigma)$ as

$$V(W; \sigma_W, \sigma_i) = N(W; 0, \sigma_W) * C(W; 0, \sigma_i) \quad (8)$$

The work on higher-mass stars on which we base this analysis shows that the average W velocity (μ_W) remains 0 km s^{-1} as the population is dynamically heated. For our sample, μ_W is close to 0 km s^{-1} as well (Table 6). Due to the small number of objects in our long-period bins, we fix $\mu_W = 0$. We choose a Cauchy over a Gaussian distribution to represent measurement errors in order to decrease the sensitivity of the model to outliers (a measurement might be an outlier if, for example, our period measurement is erroneous or if the object is an unidentified multiple).

We approximate the Voigt PDF following Thompson et al. (1987) as $(1-\eta)\,N(W; 0, \Gamma) + \eta\,C(W; 0, \Gamma)$. The parameters η and Γ depend on σ_W and σ_i; they are given in Thompson et al. (1987) and also reproduced in Ida et al. (2000). The likelihood is then an analytic function that we evaluate at each datum.

We calculate the log of $p(D|\sigma_W)$ for a grid of σ_W in step sizes of 0.1 km s^{-1}, and select the σ_W that results in the highest posterior probability. We use a bootstrap analysis to estimate errors, sampling with replacement from our data over 100 iterations.

Our approach should be insensitive to the stars missing from our sample due to MEarth's selection criteria. To test this, we also fit a generative, non-analytic model. In this case, our model is the binned distribution of a random sample of 200000 stars drawn as discussed in Section 6.1 and subject to the proper motion limit of MEarth. While we are interested only in σ_W, the velocity dispersions of the other velocity components are not independent so we fix σ_U and σ_V in the ratios of the thin disk. After drawing our sample, we apply the proper motion limit of $0\farcs15$/yr. As we demonstrated in Section 6.1, the selection of our sample using proper motions causes our sample to be missing 11% of the stars, but the fraction of stars missing will be larger when the velocity dispersion is smaller. We then convolve the resulting PDF with a Cauchy distribution to account for the errors on each datum. The results from this approach are similar to those from the simpler method we adopt.

We divide the sample into bins in period, $P < 1$ day, $1 < P < 10$ days, $10 < P < 70$ days, and $P > 70$ days, considering only objects with $0.1 < M < 0.25\,M_\odot$. Considering all rotators (both grades A and B), we infer mean ages of (0.5, 0.7, 0.6, 5.1) Gyr in these bins, respectively. We arrive at similar results using $2.3 < MEarth - K < 3.3$ to select our low-mass sample.

We also apply the relation of Wielen (1977) as described in Reiners & Basri (2009). 2MASS J06052936+6049231, the rapidly rotating star with a very negative U velocity seen in Figure 14, strongly affected the results and was excluded. The ages we infer considering all rotators for the four bins defined above are (0.7, 1.7, 3.1, 5.4) Gyr. These ages *are* affected by our proper motion bias since they rely on calculating the dispersions of the observed sample.

We present our results in Table 6. Within the errors, stars with $P < 10$ days have $\sigma_W \lesssim 10$ km s^{-1}, implying ages of <1 Gyr according to our chosen age–velocity relation. This is younger than the youngest bin used in the calibration, and the distribution of velocities in the GCS is fairly constant from 1 to 2 Gyr. We therefore assign this population of stars mean ages of $\lesssim$2 Gyr. Our results for $10 < P < 70$ days are not robust: there are relatively few stars at these periods, there is a strong dependence on the upper period boundary, and the total space velocities indicate an older population than the W component alone. For the longest-period rotators, with $P > 70$ days, we adopt a mean age of 5^{+4}_{-2} Gyr.

The velocity dispersions we determine are slightly lower than those from West et al. (2015), which is also based on the sample of MEarth rotators, and therefore we obtain slightly younger ages than one would infer from their work. Due to the mass dependence of rotational evolution (see Section 8), we restricted the range of masses used in this analysis. If we include rotators regardless of mass, we arrive at slightly larger velocity dispersions. Our work also includes a compilation of other published RVs, so more precise measurements are available for some objects, and we have made efforts to remove possible multiples, which may have velocities or periods uncharacteristic of otherwise similar stars. We also only use stars with trigonometric distance measurements.

8. THE MASS–PERIOD RELATION

Rotation is found to be strongly mass-dependent in young open clusters, with the lowest-mass stars reaching the fastest rotation rates and maintaining rapid rotation for longer. Rotational evolution at field ages is also mass-dependent. Lower-mass stars spin down more slowly than higher-mass stars on the main sequence, but eventually reach longer rotation

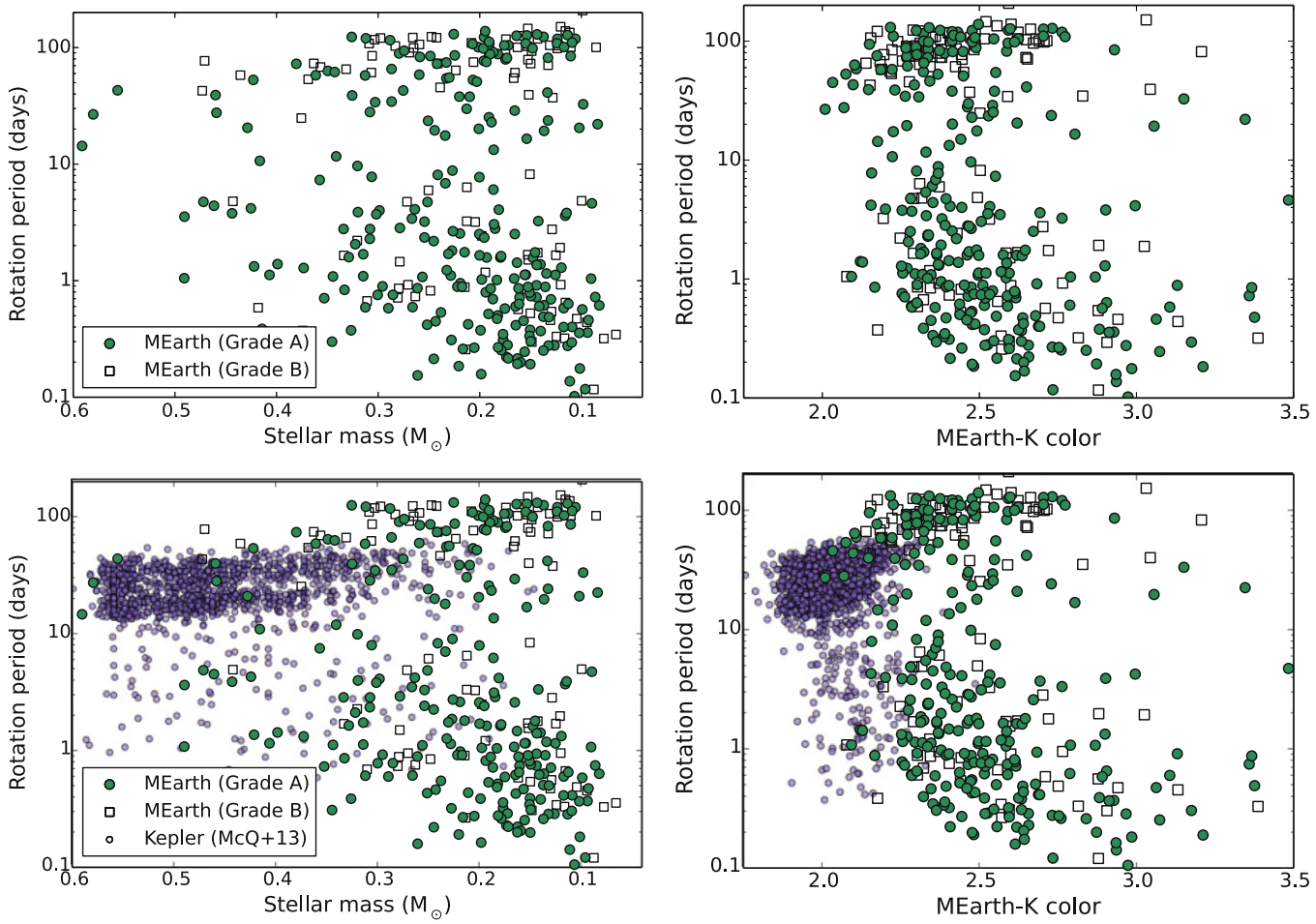

Figure 15. Period vs. stellar mass (left panels) and vs. color (right panels). Only MEarth rotators from this work are shown in the upper panels, while in the lower panels we include *Kepler* rotators from McQuillan et al. (2013) and MEarth rotators. The masses of the *Kepler* stars are estimated from broadband colors and stellar models, while the masses for the MEarth stars are estimated from absolute K magnitudes. We use a linear combination of i and z magnitudes to estimate the magnitude of the *Kepler* stars in the MEarth bandpass. We have removed known and suspected multiples from these plots, but the MEarth stars with $M > 0.3\ M_\odot$ are more likely to be unresolved multiples due to MEarth's selection criteria. We see evidence for both a lower and an upper envelope on the detected periods in the MEarth sample, and a lack of stars with intermediate rotation periods.

periods. This mass dependence in the upper envelope of rotation periods is clearly seen in Irwin et al. (2011, mid and late M dwarfs from MEarth) and McQuillan et al. (2013, 2014, early M dwarfs from *Kepler*).

We draw on the large sample of M dwarf photometric rotation periods measured from the *Kepler* survey by McQuillan et al. (2013) to explore the distribution of rotation periods across the M dwarf spectral class. We downloaded additional data on these stars from the *Kepler* Input Catalog (Brown et al. 2011, KIC) from the MAST.

Absolute magnitudes provide the best way to estimate masses for single M dwarfs, and we use parallaxes to obtain absolute K magnitudes for the MEarth rotators as described in Section 3.1. Parallaxes are not available for the majority of M dwarfs targeted by *Kepler*, so we instead use masses estimated by Dressing & Charbonneau (2013), who matched broadband photometry to Dartmouth stellar models.[6] Because the masses for MEarth and *Kepler* are determined using different methods, there may be an offset between the two mass scales. MEarth stars were selected to have $R < 0.33\,R_\odot$, so any star with a mass greater than about $0.3\,M_\odot$ is brighter than expected and more likely to be an unresolved multiple. Figure 15 plots photometric period versus estimated mass across the entire M spectral class.

Because we are interested in the mass–period relation, it is important that we have a uniform basis on which to compare the MEarth and *Kepler* samples. We therefore turn to photometric colors. The only reliable optical magnitude available for all MEarth M dwarfs is the apparent magnitude in the MEarth bandpass, which was calibrated by Dittmann et al. (2016), so we use $MEarth - K$ colors. The MEarth bandpass comprises most of i and all of z, so it is possible to estimate *MEarth* magnitudes for the *Kepler* stars from the KIC photometry with reasonable accuracy. We use an empirical relation derived from Dittman (2016) observations that we have obtained of a number of MEarth targets in the SDSS filters:

$$MEarth = (i + 2 \times z)/3 - 0.20. \quad (9)$$

This relation has a scatter of about 5%. Masses from Dressing & Charbonneau (2013) account for reddening; our color transformation does not. Figure 15 also plots photometric rotation period versus color.

[6] The requisite multicolor photometry for this method is not available for the brighter MEarth M dwarfs.

The long rotation periods we find for the mid M dwarfs are consistent with the previous MEarth results from Irwin et al. (2011), who found that the lower the mass of the star, the longer the period to which it spins down. It is challenging to infer the shape of the upper period envelope due to the lack of overlap between the stellar populations probed by *Kepler* and those probed by MEarth. McQuillan et al. (2013) did not detect rotation periods longer than 70 days in any of their objects, although they searched for periods as long as 155 days.[7] However, it is possible that *Kepler*'s systematics, particularly differences between *Kepler*'s data quarters, affect the recovery of longer rotation periods.

The lower envelope of the period distribution (shortest period seen at a given mass) is also mass-dependent, with the most rapid rotators having shorter periods at lower masses, particularly below the full convection limit. This feature is also seen in the Hyades and Praesepe open clusters (e.g., Agüeros et al. 2011) and in $v \sin i$ studies of field late M and brown dwarfs (Mohanty & Basri 2003; Jenkins et al. 2009).

We find stars with intermediate rotation periods less often than more slowly rotating stars, and that the gap between "slow" and "fast" rotators increases with decreasing mass. Using 41 light curves from the 2008–2010 seasons of MEarth data, we showed in Irwin et al. (2011) that completeness was independent of rotation period for $P < 100$ days. This implies that the gap is astrophysical. Returning to Figure 3, which shows the distribution of periods for stars in our statistical sample, the lack of stars at intermediate periods is clear in the grade A and grade B rotators, as well as in the candidate periods for the "possible" detections. A similar gap has been seen in activity studies of M dwarfs (Herbst & Miller 1989; Gizis et al. 2002; Cardini & Cassatella 2007; Browning et al. 2010).

We suggest that the most likely explanation for the gap is that these mid M dwarfs spin down rapidly from "fast" to "slow" rotation rates. Under this hypothesis, M dwarfs spend comparatively little time at intermediate rotation periods, making it unlikely that we would catch them there by chance in a field population with a wide range of ages.

9. SUMMARY

We have searched for photometric rotation periods in every star that has been observed by the northern MEarth transit survey. The rotation periods and ratings we present here supersede those reported previously in Irwin et al. (2011) and West et al. (2015). The comparison of our rotation periods to other photometric periods from the literature and to $v \sin i$ measurements lends support to the periods we have detected, although we refer the reader to Section 4 for further discussion.

The rotation periods we detect range from 0.1 to 140 days. Due to our requirement that the photometric modulation be repeated, we expect that we may not be able to detect periods greater than 140 days (about half of the longest possible observing season), so this limit may simply reflect the longest period to which we are sensitive. For fully convective stars with detected rotation periods, the amplitude of variability is independent of the rotation period, and we find no correlation between metallicity and rotation period or amplitude. Among rapid rotators, we find an abundance of stable, sinusoidal modulations. Our recovery rate in the subset of best-observed stars is $(47 \pm 5)\%$, and is higher for kinematically young stars than for kinematically old stars.

We used the variety of data that our team has collected on these stars to probe the Galactic kinematics of mid M stars in the solar neighborhood and of rotators in particular. Accounting for the selection criteria for the MEarth sample, we found that the nearby mid M dwarfs have kinematics consistent with those of higher-mass stars. We found evidence of the substructure seen in the kinematics of higher-mass stars among the M dwarfs as well, in particular the dynamically created Hyades supercluster. These substructures, which most strongly affect the U and V components of the space velocities, are important to consider when drawing conclusions about the kinematics of local groups of stars.

There is clear evidence for a rotation–age relation in all three velocity components. Using the dispersion in the W velocity component and established age–velocity relationships, we estimated the mean ages for different populations of rotators. Considering M dwarfs with $0.1 < M < 0.25\,M_{\odot}$, we found that stars with rotation periods less than 10 days are on average less than 2 Gyr old, while we estimate the slowest rotators to have an average age of 5^{+4}_{-2} Gyr. We find that most rotators are likely members of the thin/young disk.

The mass–period relationship, as traced by the MEarth and *Kepler* M dwarfs, confirms that mid M dwarfs spin down to longer periods than earlier M dwarfs. The fastest rotation periods we found among the field stars decrease with decreasing mass. We also see a lack of stars with intermediate rotation periods.

10. CONCLUSIONS

Our results are consistent with a scenario in which mid-type M dwarfs maintain rapid rotation (and enhanced magnetic activity) for the first several billion years of their life. At the age of the Hyades and Praesepe, M dwarfs have a range of rotation rates, with the latest-type M dwarfs having periods of <1 day (Scholz & Eisloffel 2007). Our field M dwarfs with periods <10 days are likely not much older than these clusters, given their low velocity dispersion. These stars do not appear to have converged to the same narrow mass–period relationship on which more massive stars are found. Convergence erases the dependence of rotation periods on the initial conditions, which is a prerequisite for gyrochronology.

We see an increase in the dispersion of total space velocity for increasingly longer periods, demonstrating that gyrochronology is potentially feasible for mid M dwarfs at ages greater than a few gigayears and rotation periods of about 100 days, if convergence can be established. Our current sample only allows us to determine that the mean age of those M dwarfs with $P > 70$ days is about 5 Gyr. This may represent a sample that is continuing to spin down slowly, and for which rotation period increases with age. More precise constraints on the age–rotation relation at long periods are required.

Galactic kinematics is a useful tool for studying the age–rotation relation, and with a larger sample of stars will provide further constraints. However, the use of kinematics is limited by our understanding of the age–velocity relation, which at present is best calibrated from 1 to 5 Gyr. Due to the population-level approach our analysis requires, kinematics may not be able to establish whether the rotation periods of mid M stars converge. M dwarfs in multiple systems with stars of

[7] In McQuillan et al. (2014) they place an upper limit of 70 days on the periods for which they searched, but they do not in this earlier work.

determined ages, such as white dwarfs, provide another promising avenue (e.g., Morgan et al. 2012; Dhital et al. 2013; Rebassa-Mansergas et al. 2013). Observations of M dwarfs in older clusters, while potentially quite useful, are technically challenging due to the greater distances at which these clusters are found, the relative faintness of the M dwarf members, and the need to establish cluster membership, but may become feasible with future observational advances.

McQuillan et al. (2013), using *Kepler* photometry, found that early-type M dwarfs with periods less than 10 days had high amplitudes of variability and stable spot patterns. They postulated that these objects were binaries, which could also explain why no candidate planets have been found around them. Extrapolation of the period distribution of the rapidly rotating mid-type M dwarfs from MEarth indicates that the young, early-type field M dwarfs should have periods of 1–10 days. The stability that McQuillan et al. (2013) saw is also reminiscent of the well-behaved sinusoids we see in rapidly rotating, lower-mass M dwarfs. This suggests that young field stars could be a substantial component of the rapidly rotating *Kepler* M dwarf sample.

The relative lack of field mid M dwarfs with intermediate rotation periods—between about 10 and 70 days—supports the suggestion of Irwin et al. (2011) that spin-down occurs rapidly. The gap in periods is similar to that seen in the distribution of magnetic activity levels, and may be the result of the same underlying physical mechanism. The rapid evolution may occur when the stars reach a critical condition, which could be a certain rotation rate or magnetic flux. It could also relate to a change in magnetic field topology, which more effectively couples the stellar wind and magnetic field (see, e.g., Garraffo et al. 2015). The mass–period relation shown in Figure 15 suggests that the critical condition may be mass-dependent, as the gap appears to narrow at earlier spectral types. Using the mean ages of our rapid and slow rotators as the lower and upper bounds, we suggest that this occurs between 2 and 5 Gyr.

The active lifetime of mid and late M dwarfs is plausibly associated with the rapid evolution we discuss above. West et al. (2015) found that the fraction of active stars (as traced through Hα emission) decreases significantly for the longest-period rotators in the MEarth sample. West et al. (2008) determined that activity lifetime is about 5 Gyr for M4V stars, and 7 Gyr for M5V stars (a large jump in active lifetime is seen between M3V and M5V, which these authors associate with the fully convective boundary). Our work implies a somewhat shorter active lifetime, but this may be the result of the different age–velocity relationship used by West et al. (2008), which assumes a steeper power law and no saturation.

Stars with rotation periods of around 100 days are not generally found to be magnetically active (West et al. 2015). Nevertheless, many slowly rotating mid-to-late M dwarfs show variability amplitudes of half a per cent or more, implying that they have maintained strong enough magnetic fields to produce the requisite spot contrasts. The lack of correlation between rotation period and amplitude for these stars indicates that the spot contrast is not changing significantly, even while they undergo substantial spin-down.

We are collecting additional Hα measurements and RVs to further improve our understanding of the connection of magnetic activity and kinematics to rotation, and using the MEarth-South data to search for new rotators among the nearby M dwarfs in the Southern Hemisphere. Our goal is to further constrain the age–rotation–activity relation, particularly at intermediate and long periods.

The MEarth project acknowledges funding from the National Science Foundation under grants AST-0807690, AST-1109468, and AST-1004488 (Alan T. Waterman Award) and the David and Lucile Packard Foundation Fellowship for Science and Engineering. This publication was made possible through the support of a grant from the John Templeton Foundation. The opinions expressed here are those of the authors and do not necessarily reflect the views of the John Templeton Foundation. E.R.N. was supported by the NSF Graduate Research Fellowship, and Z.K.B.-T. by the MIT Torres Fellowship for Exoplanet Research. A.A.W. acknowledges the support of NSF grants AST-1109273 and AST-1255568 and the Research Corporation for Science Advancement's Cottrell Scholarship.

This research has made use of data products from the Two Micron All Sky Survey, which is a joint project of the University of Massachusetts and the Infrared Processing and Analysis Center/California Institute of Technology, funded by NASA and the NSF; the Sloan Digital Sky Survey (SDSS); NASA's Astrophysics Data System (ADS); and the SIMBAD database and VizieR catalog access tool, at CDS, Strasbourg, France.

REFERENCES

Agüeros, M. A., Covey, K. R., Lemonias, J. J., et al. 2011, ApJ, 740, 110
Alekseev, I. Y., & Bondar, N. I. 1998, ARep, 42, 655
Aumer, M., & Binney, J. J. 2009, MNRAS, 397, 1286
Bailer-Jones, C. A. L. 2004, A&A, 419, 703
Bailey, J. I., White, R. J., Blake, C. H., et al. 2012, ApJ, 749, 16
Barnes, J. R., Jeffers, S. V., Jones, H. R. A., et al. 2015, ApJ, 812, 42
Barnes, J. R., Jenkins, J. S., Jones, H. R. A., et al. 2012, MNRAS, 424, 591
Barnes, J. R., Jenkins, J. S., Jones, H. R. A., et al. 2014, MNRAS, 439, 3094
Barnes, S. A. 2003, ApJ, 586, 464
Basri, G., Mohanty, S., Allard, F., et al. 2000, ApJ, 538, 363
Bayless, A. J., & Orosz, J. A. 2006, ApJ, 651, 1155
Bell, C. P. M., Rees, J. M., Naylor, T., et al. 2014, MNRAS, 445, 3496
Bensby, T., Feltzing, S., & Lundstrm, I. 2003, A&A, 410, 527
Bensby, T., Feltzing, S., Lundstrm, I., & Ilyin, I. 2005, A&A, 433, 185
Berta, Z. K., Irwin, J., Charbonneau, D., Burke, C. J., & Falco, E. E. 2012, AJ, 144, 145
Blake, C. H., Charbonneau, D., & White, R. J. 2010, ApJ, 723, 684
Borucki, W. J., Koch, D., Basri, G., et al. 2010, Sci, 327, 977
Bouvier, J., Wichmann, R., Grankin, K., et al. 1997, A&A, 318, 495
Bovy, J., & Hogg, D. W. 2010, ApJ, 717, 617
Bovy, J., Rix, H.-W., & Hogg, D. W. 2012, ApJ, 751, 131
Boyajian, T. S., von Braun, K., van Belle, G., et al. 2012, ApJ, 757, 112
Brown, T. M., Latham, D. W., Everett, M. E., & Esquerdo, G. A. 2011, AJ, 142, 112
Browning, M. K. 2008, ApJ, 676, 1262
Browning, M. K., Basri, G., Marcy, G. W., West, A. A., & Zhang, J. 2010, AJ, 139, 504
Cardini, D., & Cassatella, A. 2007, ApJ, 666, 393
Chabrier, G., & Baraffe, I. 1997, A&A
Chabrier, G., & Küker, M. 2006, A&A, 446, 1027
Charbonneau, P. 2005, LRSP, 2, 2
Chereul, E., Creze, M., & Bienayme, O. 1998, A&A, 340, 384
Chereul, E., Creze, M., & Bienayme, O. 1999, A&AS, 135, 5
Cohen, O., Drake, J. J., Glocer, A., et al. 2014, ApJ, 790, 57
Collier Cameron, A., Campbell, C. G., & Quaintrell, H. 1995, A&A, 298, 133
Curran, P. A. 2014, arXiv:1411.3816
Davenport, J. R. A., Hebb, L., & Hawley, S. L. 2015, ApJ, 806, 212
Davison, C. L., White, R., Henry, T., et al. 2015, AJ, 149, 106
De Simone, R. S., Wu, X., & Tremaine, S. 2004, MNRAS, 350, 627
Dehnen, W. 1998, AJ, 115, 2384
Delfosse, X., Forveille, T., Perrier, C., & Mayor, M. 1998, A&A, 331, 581
Delfosse, X., Forveille, T., Ségransan, D., et al. 2000, A&A, 364, 217

Deshpande, R., Blake, C. H., Bender, C. F., et al. 2013, AJ, 146, 156
Deshpande, R., Martín, E. L., Montgomery, M. M., et al. 2012, AJ, 144, 99
Dhital, S., Oswalt, T., Muirhead, P., et al. 2013, arXiv:1309.1172
Dittmann, J. A. 2016, PhD thesis, Harvard University
Dittmann, J. A., Irwin, J. M., Charbonneau, D., & Berta-Thompson, Z. K. 2014, ApJ, 784, 156
Dittmann, J. A., Irwin, J. M., Charbonneau, D., & Newton, E. R. 2016, ApJ, submitted
Dobler, W., Stix, M., & Brandenburg, A. 2006, ApJ, 638, 336
Donati, J.-F., Morin, J., Petit, P., et al. 2008, MNRAS, 390, 545
Dressing, C. D., & Charbonneau, D. 2013, ApJ, 767, 95
Eggen, O. J. 1958, MNRAS, 118, 65
Eggen, O. J. 1992, AJ, 104, 1482
Faherty, J. K., Burgasser, A. J., Cruz, K. L., et al. 2009, AJ, 137, 1
Famaey, B., Jorissen, A., Luri, X., et al. 2005, A&A, 430, 165
Famaey, B., Pont, F., Luri, X., et al. 2007, A&A, 461, 957
Famaey, B., Siebert, A., & Jorissen, A. 2008, A&A, 483, 453
Fuhrmeister, B., & Schmitt, J. H. M. M. 2004, A&A, 420, 1079
Garraffo, C., Drake, J. J., & Cohen, O. 2015, ApJ, 813, 40
Gáspár, A., Rieke, G. H., Su, K. Y. L., et al. 2009, ApJ, 697, 1578
Gizis, J. E., Reid, I. N., & Hawley, S. L. 2002, AJ, 123, 3356
Goulding, N. T., Barnes, J. R., Pinfield, D. J., et al. 2013, MNRAS, 427, 3358
Hartman, J. D., Bakos, G. A., Kovács, G., & Noyes, R. W. 2010, MNRAS, 408, 475
Hartman, J. D., Bakos, G. A., Noyes, R. W., et al. 2011, AJ, 141, 166
Hartmann, L., & Stauffer, J. R. 1989, AJ, 97, 873
Herbst, W., & Miller, J. R. 1989, AJ, 97, 891
Hoaglin, D. C., Mosteller, F., & Tukey, J. W. 1983, Understanding Robust and Exploratory Data Anlysis (New York: Wiley)
Holmberg, J., Nordström, B., & Andersen, J. 2009, A&A, 501, 941
Houdebine, E. R. 2008, MNRAS, 390, 1081
Houdebine, E. R. 2010, MNRAS, 407, 1657
Houdebine, E. R. 2012, MNRAS, 421, 3180
Houdebine, E. R., & Mullan, D. J. 2015, ApJ, 801, 106
Ida, T., Ando, M., & Toraya, H. 2000, JApCr, 33, 1311
Irwin, J., Aigrain, S., Hodgkin, S., et al. 2006, MNRAS, 370, 954
Irwin, J., Berta, Z. K., Burke, C. J., et al. 2011, ApJ, 727, 56
Irwin, J. M., Berta-Thompson, Z. K., Charbonneau, D., et al. 2014, in Proc. Conf. 767, 18th Cambridge Workshop on Cool Stars, Stellar Systems, and the Sun, ed. G. van Belle, & H. C. Harris
Jackson, R. J., & Jeffries, R. D. 2013, MNRAS, 431, 1883
Jenkins, J. S., Ramsey, L. W., Jones, H. R. A., et al. 2009, ApJ, 704, 975
Johns-Krull, C. M., & Valenti, J. A. 1996, ApJL, 459, L95
Johnson, D. R. H., & Soderblom, D. R. 1987, AJ, 93, 864
Jones, H. R. A., Pavlenko, Y., Viti, S., et al. 2005, MNRAS, 358, 105
Jurić, M., Ivezić, Ž., Brooks, A., et al. 2008, ApJ, 673, 864
Kawaler, S. D. 1988, ApJ, 333, 236
Kiraga, M. 2012, AcA, 62, 67
Kiraga, M., & Stępień, K. 2007, AcA, 57, 149
Kiraga, M., & Stępień, K. 2013, AcA, 63, 53
Koch, D., Borucki, W., Basri, G., et al. 2010, ApJL, 713, L79
Koenigl, A. 1991, ApJL, 370, L39
Konopacky, Q., Ghez, A., Fabrycky, D., et al. 2012, ApJ, 750, 79
Lépine, S. 2005, AJ, 130, 1680
Lépine, S., & Shara, M. M. 2005, AJ, 129, 1483
Malo, L., Artigau, E., Doyon, R., et al. 2014, ApJ, 788, 81
Mamajek, E. E., Bartlett, J., Seifahrt, A., et al. 2013, AJ, 146, 154
Marcy, G. W., & Chen, G. H. 1992, ApJ, 390, 550
Matt, S., & Pudritz, R. E. 2005, ApJL, 632, L135
McQuillan, A., Aigrain, S., & Mazeh, T. 2013, MNRAS, 432, 1203
McQuillan, A., Mazeh, T., & Aigrain, S. 2014, ApJS, 211, 24
Meibom, S., Barnes, S. A., Platais, I., et al. 2015, Natur, 517, 589
Meibom, S., & Mathieu, R. D. 2005, ApJ, 620, 970
Meibom, S., Barnes, S., Latham, D., et al. 2011, ApJL, 733, L9
Messina, S., Desidera, S., Lanzafame, A. C., Turatto, M., & Guinan, E. F. 2011, A&A, 532, A10
Minchev, I., Martig, M., Streich, D., et al. 2015, ApJL, 804, L9
Mohanty, S., & Basri, G. 2003, ApJ, 583, 451
Morgan, D. P., West, A. A., Garcés, A., et al. 2012, AJ, 144, 93
Morin, J., Donati, J., Petit, P., et al. 2008, MNRAS, 390, 567
Newton, E. R., Charbonneau, D., Irwin, J., et al. 2014, AJ, 147, 20
Newton, E. R., Charbonneau, D., Irwin, J., & Mann, A. W. 2015, ApJ, 800, 85
Nordstrom, B., Mayor, M., Andersen, J., et al. 2004, A&A, 418, 989
Norton, A. J., Wheatley, P., West, R., et al. 2007, A&A, 467, 785
Nutzman, P., & Charbonneau, D. 2008, PASP, 120, 317
Ofek, E. O. 2009, PASP, 121, 814
Perryman, M., Lindegren, L., Kovalevsky, J., et al. 1997, A&A, 323, L49
Perryman, M. A. C., Brown, A. G. A., Lebreton, Y., et al. 1998, A&A, 331, 40
Quillen, A. C., & Minchev, I. 2005, AJ, 130, 576
Rappaport, S., Swift, J., Levine, A., et al. 2014, ApJ, 788, 114
Rebassa-Mansergas, A., Schreiber, M. R., & Gansicke, B. T. 2013, MNRAS, 429, 3570
Reid, I. N., Kirkpatrick, J. D., Liebert, J., et al. 2002, AJ, 124, 519
Reiners, A., & Basri, G. 2007, ApJ, 656, 1121
Reiners, A., & Basri, G. 2008, ApJ, 684, 1390
Reiners, A., & Basri, G. 2009, ApJ, 705, 1416
Reiners, A., & Basri, G. 2010, ApJ, 710, 924
Reiners, A., Joshi, N., & Goldman, B. 2012a, AJ, 143, 93
Reiners, A., & Mohanty, S. 2012b, ApJ, 746, 43
Robb, R. M., Balam, D. D., & Greimel, R. 1999, IBVS, 4714, #1
Saar, S. H., Butler, R. P., & Marcy, G. W. 1998, ApJL, 498, L153
Saar, S. H., & Donahue, R. A. 1997, ApJ, 485, 319
Schmidt, S. J., Cruz, K. L., Bongiorno, B. J., Liebert, J., & Reid, I. N. 2007, AJ, 133, 2258
Scholz, A., & Eisloffel, J. 2007, MNRAS, 381, 1638
Scholz, F. W., & Stephens, M. A. 1987, J. Am. Stat. Assoc., 82, 918
Schönrich, R., Binney, J., & Dehnen, W. 2010, MNRAS, 403, 1829
Schweitzer, A., Gizis, J. E., Hauschildt, P. H., Allard, F., & Reid, I. N. 2001, ApJ, 555, 368
Seabroke, G. M., & Gilmore, G. 2007, MNRAS, 380, 1348
Shkolnik, E. L., Hebb, L., Liu, M. C., Neill Reid, I., & Cameron, A. C. 2010, ApJ, 716, 1522
Skumanich, A. 1972, ApJ, 171, 565
Smith, J., Stumpe, M., Van Cleve, J., et al. 2012, PASP, 124, 1000
Soubiran, C., Bienaymé, O., Mishenina, T. V., & Kovtyukh, V. V. 2008, A&A, 480, 91
Stauffer, J. R., & Hartmann, L. W. 1986, ApJS, 61, 531
Stauffer, J. R., Hartmann, L. W., & Latham, D. W. 1987, ApJL, 320, L51
Stauffer, J. R., Hartmann, L. W., Prosser, C. F., et al. 1997, ApJ, 479, 776
Stumpe, M., Smith, J., Van Cleve, J., et al. 2012, PASP, 124, 985
Tanner, A., White, R., Bailey, J., et al. 2012, ApJS, 203, 10
Thompson, P., Cox, D. E., & Hastings, J. B. 1987, JApCr, 20, 79
Tinney, C. G., & Reid, I. N. 1998, MNRAS, 301, 1031
Tokovinin, A. A. 1992, A&A, 256, 121
Torres, C. A. O., Quast, G. R., da Silva, L., et al. 2006, A&A, 460, 695
Vogt, S. S., Penrod, G. D., & Soderblom, D. R. 1983, ApJ, 269, 250
West, A. A., & Basri, G. 2009, ApJ, 693, 1283
West, A. A., Hawley, S. L., Bochanski, J. J., et al. 2008, AJ, 135, 785
West, A. A., Weisenburger, K. L., Irwin, J., et al. 2015, ApJ, 812, 3
Wielen, R. 1977, A&A, 60, 263
Winters, J. 2015, Nearby Red Dwarfs and Their Dance Partners: Characterizing More Than 2000 Single and Multiple M Dwarfs Near the Sun
Yadav, R. K., Christensen, U. R., Morin, J., et al. 2015, ApJL, 813, L31
Zapatero Osorio, M. R., Martin, E. L., Bouy, H., et al. 2006, ApJ, 647, 1405
Zickgraf, F.-J., Krautter, J., Reffert, S., et al. 2005, A&A, 433, 151